IEEE Access
Multidisciplinary ⋮ Rapid Review ⋮ Open Access Journal

Received 3 March 2023, accepted 14 March 2023, date of publication 22 March 2023, date of current version 29 March 2023.

Digital Object Identifier 10.1109/ACCESS.2023.3260645

RESEARCH ARTICLE

A New Proposal Generalized Predictive Control Algorithm With Polynomial Reference Tracking Applied for Sodium Fast Reactors

LUÍS FELIPE DA SILVA CARLOS PEREIRA[1], EDSON ANTONIO BATISTA[1], (Member, IEEE), JOÃO ONOFRE PEREIRA PINTO[2], (Senior Member, IEEE), BELLE R. UPADHYAYA[3], AND J. WESLEY HINES[3]

[1]Faculty of Engineering, Architecture and Urban Planning and Geography, Federal University of Mato Grosso do Sul, Campo Grande 79070-900, Brazil
[2]Oak Ridge National Laboratory, Oak Ridge, TN 37830, USA
[3]University of Tennessee, Knoxville, TN 37996, USA

Corresponding author: Edson Antonio Batista (edson.batista@ufms.br)

ABSTRACT This paper proposes a generalized predictive control (GPC) with constraints and orthonormal Laguerre functions using the simplified model of the primary system (reactor core and intermediate heat exchanger (IHX)) of a prototypical sodium fast reactor (SFR). This paper develops a multiple-input multiple-output (MIMO) GPC with input constraints able to track polynomial references of any degree applied in coolant temperature difference across the core and fractional power. The manipulated variables of the GPC-SFR are the reactivity and the sodium flow rate of the primary and secondary pipes. Moreover, orthonormal Laguerre functions and step down condition number techniques were also applied to avoid the numerical ill-conditioning issue in quadratic programming of large systems. Thus, a GPC type-2 was designed to control fractional power, coolant temperature difference across the core and sodium tank temperature of the SFR primary system when temperature references change according to a linear ramp after reaching their steady-state operation, sustaining 100% power operation on the reactor. In order to analyze the load tracking capability of the GPC-SFR type-2, the load following from 100% fractional power (FP) to 60% FP at 0.8% FP/min rate is simulated. Constraints on the rate of coolant temperature difference across the core and reactivity were applied for the design safety. For comparison criteria, this paper compares the GPC-SFR type-2 with the GPC-SFR type-1, i.e, standard model predictive control (MPC), to verify the viability and superior performance of the proposal regarding: (a) ramp-tracking capability of temperature and load; (b) the rejections of a reactivity disturbance of -1 cent and a secondary sodium inlet temperature disturbance of $+10^{o}F$; and (c) a simulation with uncertainty in reactor design. The simulations show that the GPC-SFR type-2 overcome the GPC-SFR type-1 robustness and performance.

INDEX TERMS Generalized predictive control, orthonormal Laguerre functions, polynomial reference tracking, quadratic programming, sodium fast reactor.

I. INTRODUCTION

The control of advanced reactors faces significant technique hurdles in implementation due to the unique characteristics inherent to their designs, such as demanding huge hardware size memory, nonlinear model equations, new component designs, multiple-input multiple-output (MIMO) variables, and harsh constraint implementation. Reference [1] simulated and controlled an integral pressurized water reactor, with multiple units that operates in parallel and feed steam to a single turbine. In addition, [2] presents advanced instrumentation and control methods for small and medium reactors with IRIS demonstration.

Sodium fast reactors (SFRs) are a class of advanced reactor design that uses sodium as a coolant to remove heat from the reactor core, and transfer it to heat exchanges and steam

The associate editor coordinating the review of this manuscript and approving it for publication was Guillermo Valencia-Palomo.

generators [3]. The advanced reactor model studied in this paper is based on the Experimental Breeder Reactor - II (EBR-II) which operates with a capacity of 62.5 MWth with 20 MWe output. Many important works were developed to control SFRs with different techniques. Reference [4] performed a linear quadratic (LQR) compensator to control the fractional power, fuel temperature, reactor inlet and outlet temperatures upon -5 cent reactivity insertion. Moreover, [3] designed a traditional PI control and an optimal model predictive control (MPC) as related to core inlet temperature and temperature change across the core under a variety of reactor power levels ($30 - 100\%$ power) with external reactivity perturbations of -1 cent. The advances in research and hardware deployment for industrial applications drive the study for new control technologies in nonlinear MIMO models. Accordingly, the state-of-art literature describes intelligent controllers [5], fractional-order controllers [6] and advanced variants of LQR [7]. However, none of these presented studies can achieve either the zero steady-state error for polynomial references or the polynomial-exogenous disturbances rejection. In order to address those shortcomings, the generalized predictive control (GPC) type-m with Laguerre functions is employed in this work.

The prototypical advanced reactor (PAR) based on coolant liquid of sodium was designed primary to operate with two independent reactor cores, each connected to a dedicated intermediate heat exchanger (IHX) and steam generator [8]. The power unbalance between the core reactors due to power tilt between the upper and lower half cores can affect the overall supply of energy [9]. In order to overcome this problem, load-following power can regulate the total power. However, in a load-following circumstance, a step-back is noticed during the time interval of the power fast drop [10]. The power level variation causes irregular circumstances in control rods and sodium flow rates. As regards [11], an MPC was applied to the core power control in a Pressurized Water Reactor (PWR), and a linear load-following test was simulated. According to the type-1 control theory, the zero steady-state error through the linear power transition cannot be achieved by the proposed MPC, surging the demand of type-2 controllers for linear load tracking. According to the constraints on reactivity rate and coolant temperature difference rate across the core, the proposed GPC type-2 controls the linear load-following process with zero steady-state error to avoid a forced shut down. Recently, many works have been published as related to the core power control in [9], [10], [12], and [13]. However, those approaches provide no study regarding the control of the sodium flow rate and reactivity to aim the safety of the reactor temperature.

The demand for temperature control for SFRs reactors arises from the inherent uncertainties of several modeling parameters such as geometric dimensions and material compositions as it is impossible to cover all scenarios of computational analyses [14]. Moreover, the reactor temperature handles directly in the reactor feedback reactivity. Purposing reactor safety, negative temperature coefficients of reactivity are required such that the increase of temperature leads to a reactivity reduction and potential reactor shut down [15]. According to model uncertainties, the nonlinear reactor design must be robust to temperature changes for an operation nominal power. Primary and secondary sodium flow rates are the stipulated manipulated variables that can control the inlet and outlet reactor temperatures, i.e. sodium tank and primary plenum temperatures (core temperature). Thus, regarding the correlation between temperature and reactivity aforementioned, an external reactivity as the third manipulated variable also shows up for the purposing of maintaining operation at 100% power even with a linear temperature change of the coolant temperature difference across the core. Linear temperature change is used due to the slow dynamics of the reactor, so each change can be designed as a ramp among a small measured time.

According to output regulation, the internal model principle (IMP) states that a system is able to track input signals with a zero steady-state error if a feedback controller is chosen to provide closed-loop stability when the open-loop is written with its minimal state realization and it has at least the unstable part of the exogenous signal embedded on it [16]. By introducing a controller with the IMP in a minimal state realization system, reference [17] proposed a GPC with predicted errors and second-order difference operator in state variables as an augmented state of a single-input single-output (SISO) system for ramp-reference tracking. Owing to the non-integrator feature in the system chosen, the designer needed to add 2 integrators such that the internal mode of $1/s^2$ could be inserted into the loop, resulting in tracking with zero steady-state error. Furthermore, reference [18] extended the method in [17] by using high-order backward difference operators to achieve zero steady-state error for polynomial reference tracking. One can track polynomial reference of degree $m - 1$ of a minimal realization system without integrators embedded if m integrators are inserted into the open-loop system. Hence, high-order backward difference operators were applied in error and in system state variables to achieve augmented states with m integrators embedded. Again, the method was only developed for SISO systems, without optimized usage of GPC parameters and none prescribed stability. Regarding [19], a new approach was developed to embed an internal model of sinusoidal reference through the application of the first and second-order difference operators in a SISO system. More applications of type-m controllers ($m \geq 2$) can be found in [20], [21], [22], [23], and [24]. Despite being an interesting approach, no achievements were done concerning MIMO systems or order reduction by using orthonormal functions to extract accurately the control variable behavior. For a non-minimal realization MIMO reactor with 37 state variables, it is aimed to embed 2 integrators for ramp-reference tracking of the coolant temperature difference across the core while it is maintaining the power operation at 100 %. Besides, it is sought to achieve ramp-reference tracking of the fractional power and the coolant temperature difference across the

core while it is controlled the tank temperature. For this purpose, as high-order systems are a burden for practical applications, orthonormal Laguerre functions with prescribed stability were employed to design the MIMO GPC type-m in this paper.

Laguerre functions are widely used for system identification through their orthonormal basis functions [25] and [26]. In [27], the Laguerre basis expansion was used for a linear parameter-varying (PV) Hammerstein method with low-pass dynamics and its application was extended to nonlinear PV Hammerstein identification. The main achievement of using Laguerre functions was decreasing the number of impulse response function parameters by 82.41 %. In addition, Laguerre functions can also solve the challenge of decreasing the high MPC processing cost with a choice of a few functions without compromising the dynamic performance of the system [28]. Thus, aiming for matrices size reduction of the linearized nuclear reactor, orthonormal Laguerre functions were applied to the augmented control variables proposed.

The objective of this paper is to develop a MIMO GPC, with orthonormal Laguerre functions and constraints, capable to track polynomial references of an arbitrary degree $m-1$ in SFR. It is worth mentioning that this method can be underwent under any electro-mechanical under-actuated systems. For practical application, a GPC type-2 is designed to overcome a GPC type-1 for: (a) disturbance rejection in reactivity and secondary sodium inlet temperature; (b) ramp-power tracking and ramp-temperature tracking; and (c) uncertainty in reactor parameters. The Mean Squared Error (MSE) is the performance index to feature the best controller. To design this controller, the nonlinear system was developed using MATLAB/Simulink. This paper generalized the control theory presented in [18] through MIMO systems with the enhancement regarding the condition number of systems with huge state-space matrices and the order reduction of Hessian matrix by orthonormal Laguerre functions in control variables without loss of dynamical responses.

This paper is organized as follows. Section II shows ERB-II-CORE and Intermediate Heat Exchanger (IHX) dynamical equations as related to all input and output variables. Section III presents the proposed MIMO GPC type-m along with its Laguerre orthonormal function application. Section IV demonstrates the proposed control approach for the Prototypical SFR along with the setup parameters of the GPC type-2 when loading input constraints. An algorithm is proposed as well. Section V includes simulations and results comparing the GPC-SFR type-1 with the GPC-SFR type-2 when measured and unmeasured disturbances are applied. Consequently, the simulations of load and temperature tracking are assessed as well. Concluding remarks are stated in Section VI.

II. ERB-II-CORE AND THE INTERMEDIATE HEAT EXCHANGER (IHX) MODELING

The primary system consists of the following: (a) reactor, (b) primary cooling systems, (c) neutron shield, (d) fuel handling system, (e) control and safety drive systems, (f) tank and biological shield, (g) fuel unloading and inter-building transfer, (h) primary sodium purification system, and (i) argon blanket gas system. For the purpose of PAR model, only the reactor and primary cooling system are modeled. A node formulation, of the primary loop and the IHX, is presented in Figure 1 and the state-variable names of the Upadhyaya's model on each node are presented in [29]. The primary loop includes the active core, inner and outer blankets, lower and upper reflectors, and piping. The formulation of the whole model and all the parameters are adapted using the models in [4]. The primary loop and IHX models are coupled into one module for the convenience of simulation studies. The governing equations for each subsystem and the definition of variables are presented in the following sections. The parameter value for each constant can be found in [4].

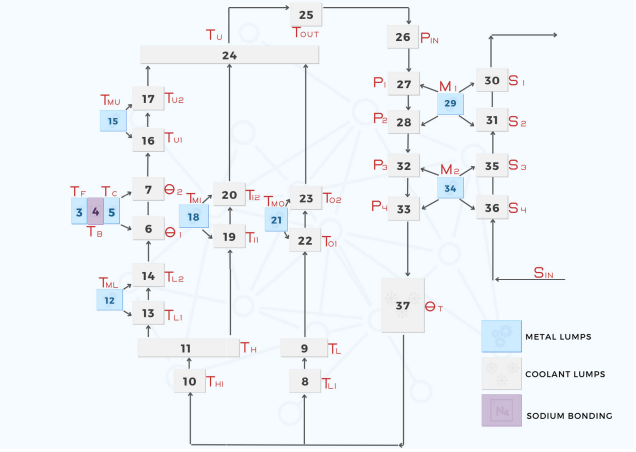

FIGURE 1. Node representation of EBR-II primary system [8].

The variables from 1 to 37 in Figure 1 are described as following: 1, fractional reactor power; 2, precursor concentration; 3-7, active core temperatures; 8-9, low pressure plenum temperatures; 10-11, high pressure plenum temperatures; 12-14, lower reflector temperatures; 15-17, upper reflector temperatures; 18-20, inner blankets temperatures; 21-23, outer blankets temperatures; 24, upper plenum temperature; 25-26, IHX inlet plenum temperatures; 27-36, IHX temperatures; 37, sodium tank temperature. Remark that the fractional reactor power or a percentage of its value is applied in variables 3, 12, 15, 18 and 21.

Through the ERB-II model by [4], it is used the ERB-II Core + IHX model to represent the reactor at MATLAB/Simulink with 4 inputs and 5 outputs. The inputs are given by the reactivity (ExternalReactivity), the inlet temperature of the sodium in the secondary region (Sin), the primary flow rate of sodium (Primary) and the secondary flow rate of sodium (Secondary). The outputs are the power fraction of the reactor core (Out1), the temperature in the upper part of the Plenum (Out2), the temperature in the second node of the secondary (Out3), inlet temperature of

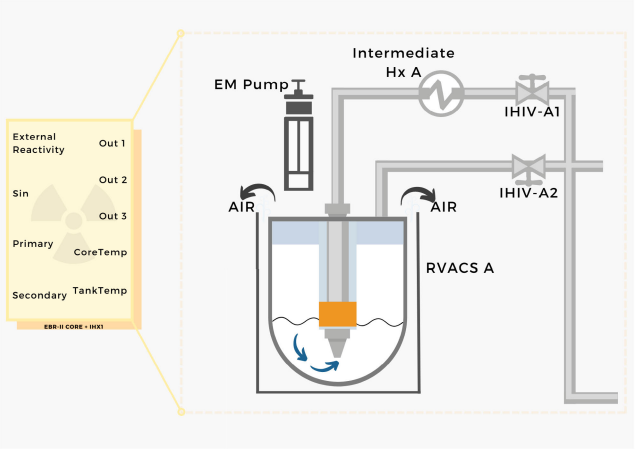

FIGURE 2. ERB-II-Core + IHX Modelling in MATLAB/Simulink.

the primary plenum (Core Temp) and the temperature of the sodium tank (Tank Temp). The block is shown in Figure 2.

A. REACTOR CORE EQUATIONS

The reactor contains the fuel material and blanket material, which are all in the reactor vessel. In addition to the fuel material, fuel bearing subassemblies consist of upper and lower axial blanket regions. The active core dynamics are described by the point reactor kinetics equations [4], with a slight modification of the reactivity feedback coefficients α_i (TABLE 1). Note that ρ_{ext} (external reactivity), S_{in} (secondary sodium inlet temperature), ϕ_1 (primary flow rate of sodium) and ϕ_2 (secondary flow rate of sodium) are introduced as nodes 38, 39, 40 and 41 in MATLAB/Simulink model, respectively.

1) NONLINEAR REACTOR KINETICS

$$\begin{aligned}\frac{dP_c}{dt} &= -\frac{\beta_T}{\Lambda}P_c + \left(\frac{\beta_T}{100}\rho_{ext} + \rho_{feedback}\right)\frac{P_c}{\Lambda} + \bar{\lambda}C;\\ \rho_{feedback} &= \sum_i \alpha_i(T_i - T_{i_0});\end{aligned} \tag{1}$$

$$\begin{aligned}\frac{dC_c}{dt} &= \frac{\beta_T}{\Lambda}\Delta P_c - \bar{\lambda}C_c;\\ C &= C_c + C_0;\\ C_0 &= \frac{\beta_T}{\Lambda\bar{\lambda}}P_{c_0};\end{aligned} \tag{2}$$

where: P_c = the fractional core power; P_{c_0} = the steady-state fractional core power; β_T = total delayed neutron fraction; Λ = neutron generation time; ρ = reactivity; $\bar{\lambda}$ = precursor average decay constant; C = precursor concentration; α_i = temperature reactivity feedback coefficient corresponding to temperature T_i; T_i = current temperature in channel i; T_{i_0} = steady-state temperature for channel i at 100% power.

2) CORE HEAT TRANSFER

Mann's model is used to represent the heat transfer dynamics. Average lump temperature is a coupling parameter for the driving force of heat transfer between the coolant and metal nodes. The lower coolant lump outlet temperature is assumed to present the average lump temperature in Mann's model [4]. Equations (3) - (7) correspond with the five lumps:

TABLE 1. α_i adjustment factor for values in [4].

Index	Value
i = 2 and 3	1/1.168
i = 4	1/83.3
i = 5	1/10.2
i = 6	1/1.1467

$$\frac{dT_F}{dt} = \frac{P_F P_0}{1.218(MC_p)_F}P_c - \frac{5640}{R_1(MC_p)_F}(T_F - T_B); \tag{3}$$

$$\frac{dT_B}{dt} = \frac{5640}{R_1(MC_p)_B}(T_F - T_B) - \frac{5640}{R_2(MC_p)_B}(T_B - T_C); \tag{4}$$

$$\frac{dT_C}{dt} = \frac{1344.1}{R_2(MC_p)_B}(T_B - T_C) - \frac{7066.9}{R_3(MC_p)_\theta}(T_B - \theta_1); \tag{5}$$

$$\frac{d\theta_1}{dt} = \frac{5640}{R_3(MC_p)_\theta}(T_C - \theta_1) + 0.003\phi_1(T_{L_2} - \theta_1); \tag{6}$$

$$\frac{d\theta_2}{dt} = \frac{5640}{R_3(MC_p)_\theta}(T_C - \theta_1) + 0.003\phi_1(\theta_1 - \theta_2); \tag{7}$$

where: T_F = fuel temperature; T_B = sodium-bond temperature; T_C = fuel cladding temperature; θ_i = temperature of the ith coolant node; R_1, R_2, R_3 = heat transfer resistances; P_F = fraction of the power deposited in the fuel; $(C_p)_F$ = specific heat capacity of the fuel; $(C_p)_B$ = specific heat capacity of the blanket material; $(C_p)_\theta$ = specific heat capacity of the coolant; M_F = mass of the fuel; M_B = mass of the blanket material; M_θ = mass of the coolant.

B. REFLECTOR AND BLANKET MODELS

In the EBR-II, reflectors and blankets surround the reactor core. The core model consists of twelve nodes representing the reflector and radial blanket region. The same heat transfer principle used in the core heat transfer model is also applied to develop the state equations. The equations for the lower, upper and inner reflectors, along with the outer blanket region are described by (8) - (19) as shown below [4]:

1) LOWER REFLECTOR

$$\frac{dT_{M_L}}{dt} = \frac{P_{i_{LU}}}{2.83(MC_p)_{M_L}}P_c - \frac{(UA)_L}{(MC_p)_{M_L}}(T_{M_L} - T_{L_1}); \tag{8}$$

$$\frac{dT_{L_1}}{dt} = \frac{(UA)_L}{(MC_p)_{T_{L_1}}}(T_{M_L} - T_{L_1}) + 0.0021\phi_1(T_H - T_{L_1}); \tag{9}$$

$$\frac{dT_{L_2}}{dt} = \frac{(UA)_L}{(MC_p)_{T_{L_2}}}(T_{M_L} - T_{L_1}) + 0.0021\phi_1(T_{L_1} - T_{L_2}); \tag{10}$$

2) UPPER REFLECTOR

$$\frac{dT_{M_U}}{dt} = \frac{10P_{i_{LU}}}{(MC_p)_{M_U}}P_c - \frac{(UA)_U}{(MC_p)_{M_U}}(T_{M_U} - T_{U_1}); \tag{11}$$

$$\frac{dT_{U_1}}{dt} = \frac{(UA)_U}{(MC_p)_{T_{U_1}}}(T_{M_U} - T_{U_1}) + 0.0021\phi_1(\theta_2 - T_{U_1}); \tag{12}$$

$$\frac{dT_{U_2}}{dt} = \frac{(UA)_U}{(MC_p)_{T_{U_2}}}(T_{M_U} - T_{U_1}) + 0.0021\phi_1(T_{U_1} - T_{U_2}); \tag{13}$$

3) INNER REFLECTOR

$$\frac{dT_{M_I}}{dt} = \frac{1.5P_{i_I}}{(MC_p)_{M_I}}P_c - \frac{(UA)_I}{(MC_p)_{M_I}}(T_{M_I} - T_{I_1}); \tag{14}$$

$$\frac{dT_{I_1}}{dt} = \frac{(UA)_I}{(MC_p)_{T_{I_1}}}(T_{M_I} - T_{I_1}) + 8.2254 \cdot 10^{-4}\phi_1(T_H - T_{I_1}); \tag{15}$$

$$\frac{dT_{I_2}}{dt} = \frac{(UA)_I}{(MC_p)_{T_{I_2}}}(T_{M_I} - T_{I_1}) + 8.2254 \cdot 10^{-4}\phi_1(T_{I_1} - T_{I_2}); \tag{16}$$

4) OUTER BLANKET

$$\frac{dT_{M_O}}{dt} = \frac{10P_{i_O}}{(MC_p)_{M_O}}P_c - \frac{(UA)_O}{(MC_p)_{M_O}}(T_{M_O} - T_{O_1}); \tag{17}$$

$$\frac{dT_{O_1}}{dt} = \frac{(UA)_O}{(MC_p)_{T_{O_1}}}(T_{M_O} - T_{O_1}) + 2.0403 \cdot 10^{-4}\phi_1(T_L - T_{O_1}); \tag{18}$$

$$\frac{dT_{O_2}}{dt} = \frac{(UA)_O}{(MC_p)_{T_{O_2}}}(T_{M_O} - T_{O_1}) + 2.0403 \cdot 10^{-4}\phi_1(T_{O_1} - T_{O_2}); \tag{19}$$

where: P_i = steady-state power of the reflectors or blanket; T_M = temperature of the metal node; T_1 = temperature of the first region coolant node; T_2 = temperature of the second region coolant node; A = total heat transfer area; U = metal to coolant heat transfer coefficient; $(C_p)_M$ = specific heat capacity of the metal; $(C_p)_T$ = specific heat capacity of the coolant.

C. PIPING AND PLENUM MODEL

The model consists of six nodes for the low and high pressure plenum, the upper plenum and core inlet-outlet piping region. A transfer-lag has been assumed for the piping. The other assumptions include constant coolant density, no heat gain or loss in the piping, and no axial heat conduction [4]. The differential equations (20) - (25) are stated below:

$$\frac{dT_U}{dt} = 1.3322 \cdot 10^{-5}\phi_1(T_{U_2} - T_U) + 3.1848 \cdot 10^{-6}\phi_1(T_{I_2} - T_U) + 2.7442 \cdot 10^{-6}\phi_1(T_{O_2} - T_U); \tag{20}$$

$$\frac{dT_{out}}{dt} = 7.2150 \cdot 10^{-5}\phi_1(T_U - T_{out}); \tag{21}$$

$$\frac{dT_{LI}}{dt} = 6.1775 \cdot 10^{-5}\phi_1(\theta_T - T_{LI}); \tag{22}$$

$$\frac{dT_{HI}}{dt} = 6.2415 \cdot 10^{-5}\phi_1(\theta_T - T_{HI}); \tag{23}$$

$$\frac{dT_H}{dt} = 7.4562 \cdot 10^{-5}\phi_1(T_{HI} - T_H); \tag{24}$$

$$\frac{dT_L}{dt} = 6.8302 \cdot 10^{-6}\phi_1(T_{LI} - T_L); \tag{25}$$

where: T_U = upper plenum temperature; T_{out} = reactor outlet temperature; θ_T = sodium tank temperature; T_{LI} = low-pressure plenum inlet temperature; T_{HI} = high-pressure plenum inlet temperature; T_H = high-pressure plenum temperature; T_L = low-pressure plenum temperature.

D. INTERMEDIATE HEAT TRANSFER

The sodium tank and primary inlet plenum are represented by transport-lag approximations. Mann's model is also used for the heat transfer between the primary and intermediate loop sodium. Twelve nodes (26) - (37) are used to represent the IHX and sodium tank as related in [4].

$$\frac{dP_1}{dt} = 5.8543 \cdot 10^{-5}\phi_1 P_{in} - (\frac{(UA)_p}{(MC_p)_p} + 6.0966 \cdot 10^{-5}\phi_1)P_1 + \frac{(UA)_p}{(MC_p)_p}M_1; \tag{26}$$

$$\frac{dP_2}{dt} = (5.8543 \cdot 10^{-5}\phi_1 - \frac{(UA)_p}{(MC_p)_p})P_1 - 6.0966 \cdot 10^{-5}\phi_1 P_2 + \frac{(UA)_p}{(MC_p)_p}M_1; \tag{27}$$

$$\frac{dM_1}{dt} = \frac{(UA)_p}{2(MC_p)_M}P_1 - (\frac{(UA)_p + (UA)_S}{2(MC_p)_M})M_1 + \frac{(UA)_S}{2(MC_p)_M}S_1; \tag{28}$$

$$\frac{dS_4}{dt} = \frac{1.083(UA)_S}{(MC_p)_S}M_2 - (\frac{(UA)_S}{(MC_p)_S} - 2.3745 \cdot 10^{-4}\phi_2)S_3 - 2.3745 \cdot 10^{-4}\phi_2 S_4; \tag{29}$$

$$\frac{dS_3}{dt} = \frac{1.083(UA)_S}{(MC_p)_S}M_2 - (\frac{(UA)_S}{(MC_p)_S} + 2.3745 \cdot 10^{-4}\phi_2)S_3 + 2.3745 \cdot 10^{-4}\phi_2 S_{in}; \tag{30}$$

$$\frac{dP_3}{dt} = 5.8543 \cdot 10^{-5}\phi_1 P_2 - (\frac{(UA)_p}{(MC_p)_p} + 6.0966 \cdot 10^{-5}\phi_1)P_3 + \frac{(UA)_p}{(MC_p)_p}M_2; \tag{31}$$

$$\frac{dP_4}{dt} = (5.8543 \cdot 10^{-5}\phi_1 - \frac{(UA)_p}{(MC_p)_p})P_3 - 6.0966 \cdot 10^{-5}\phi_1 P_4 + \frac{(UA)_p}{(MC_p)_p}M_2; \tag{32}$$

$$\frac{dM_2}{dt} = \frac{(UA)_p}{2(MC_p)_M}P_3 - (\frac{(UA)_p + (UA)_S}{2(MC_p)_M})M_2 + \frac{(UA)_S}{2(MC_p)_M}S_3; \tag{33}$$

$$\frac{dS_2}{dt} = \frac{1.083(UA)_S}{(MC_p)_S}M_1 - (\frac{(UA)_S}{(MC_p)_S} - 2.3745\cdot 10^{-4}\phi_2)S_1 - 2.3745\cdot 10^{-4}\phi_2 S_2; \quad (34)$$

$$\frac{dS_1}{dt} = \frac{1.083(UA)_S}{(MC_p)_S}M_1 - (\frac{(UA)_S}{(MC_p)_S} + 2.3745\cdot 10^{-4}\phi_2)S_1 + 2.3745\cdot 10^{-4}\phi_2 S_4; \quad (35)$$

$$\frac{dP_{in}}{dt} = 5.8173\cdot 10^{-5}\phi_1(T_{out} - P_{in}); \quad (36)$$

$$\frac{d\theta_T}{dt} = 2.0107\cdot 10^{-7}\phi_1(P_4 - \theta_T); \quad (37)$$

where: P_1 = first primary node temperature; P_2 = second primary node temperature; P_3 = third primary node temperature P_4 = fourth primary node temperature; M_1 = first (upper) tube wall temperature; M_2 = second (lower) tube wall temperature; S_1 = first secondary node temperature; S_2 = second secondary node temperature; S_3 = third secondary node temperature; S_4 = fourth secondary node temperature; P_{in} = primary inlet plenum temperature; T_{out} = reactor outlet temperature; S_{in} = secondary sodium inlet temperature.

Regarding (1) and (2), the reactor primary system is highly nonlinear. Thus, the reactor model was build in MATLAB/Simulink with the equations (1)-(37) to aim more reliable simulations. The insertion of primary and secondary flow rates of sodium also steps up the system nonlinearity as it can seen in (6)-(7), (9)-(10), (12)-(13), (15)-(16), (18)-(19), (20)-(27), (29)-(32) and (34)-(37). In order to design the GPC, the system must be linearized at some operating point for building the state-space matrices. Reference [29] describes the arrangement and steady-state values of the state variables for the system when it operates at 100% power. The Model Linearizer toolbox of MATLAB/Simulink was employed to find the continuous state-space matrices of the SFR. The non-zero entry elements of the continous space-state matrices A, B and C are presented in appendix A. A sampling time $T_s = 1$ second was used to discretize the state-space matrices for using in the GPC with the MATLAB's function "c2dm". It is worth mentioning that the obtained linearization generated a non-minimal state realization. Finally, the GPC was inserted to control the nonlinear model.

III. PROPOSED GPC MIMO SYSTEM

A. PROPOSED AUGMENTED PREDICTION MODEL

Consider the following n_1-order discrete MIMO plant:

$$\begin{aligned} x_m(i+1) &= Ax_m(i) + Bu_m(i), \\ y_m(i) &= Cx_m(i), \end{aligned} \quad (38)$$

where $x_m \in \mathbb{R}^{n_1\times 1}$, $A \in \mathbb{R}^{n_1\times n_1}$, $B \in \mathbb{R}^{n_1\times n_{in}}$, $u_m \in \mathbb{R}^{n_{in}\times 1}$, $C \in \mathbb{R}^{m_1\times n_1}$ and $y_m \in \mathbb{R}^{m_1\times 1}$. In other words, the plant has n_{in} inputs, m_1 outputs and n_1 states. Defining the track error $e(i)$, where $r(i)$ is the reference applied upon the system, as:

$$e(i) = r(i) - y_m(i), \quad (39)$$

one can use the m^{th}-order backward difference operator (∇^m) [18] into (38) and in a step beyond of (39) to find:

$$\begin{aligned} \nabla^m x_m(i+1) &= A\nabla^m x_m(i) + B\nabla^m u_m(i), \\ \nabla^m e(i+1) &= \nabla^m r(i+1) - C\nabla^m x_m(i+1), \\ &= \nabla^m r(i+1) - CA\nabla^m x_m(i) - CB\nabla^m u_m(i) \end{aligned} \quad (40a)$$

As regards [18], through the polynomial reference tracking, $\nabla^m r(i+1) = 0$, thus (40a) yields in:

$$\nabla^m e(i+1) = -CA\nabla^m x_m(i) - CB\nabla^m u_m(i). \quad (41)$$

Let $a_j = \nabla^{m-j}e(i+1)$. According to the telescoping sum property, $\sum_{j=1}^{g}(a_j - a_{j-1}) = a_g - a_0$ [30]. Moreover $\nabla^{m-(j-1)}e(i+1) = \nabla^{m-j}e(i+1) - \nabla^{m-j}e(i)$. Hence, $a_j - a_{j-1} = \nabla^{m-j}e(i+1) - \nabla^{m-(j-1)}e(i+1) = \nabla^{m-j}e(i)$. Through these results, $\nabla^{m-g}e(i+1)$ can be found as in (42):

$$\underbrace{\nabla^{m-g}e(i+1)}_{a_g} = \underbrace{\nabla^m e(i+1)}_{a_0} + \sum_{j=1}^{g}\underbrace{\nabla^{m-j}e(i)}_{a_j - a_{j-1}}. \quad (42)$$

Replacing (41) into (42), yields:

$$\nabla^{m-g}e(i+1) = -CA\nabla^m x_m(i) - CB\nabla^m u_m(i) + \sum_{j=1}^{g}\nabla^{m-j}e(i). \quad (43)$$

Let $\varkappa(i) = [\underbrace{e_1(t),\cdots,e_{m_1}(t)}_{e(t)}, \underbrace{\nabla e_1(t),\cdots,\nabla e_{m_1}(t)}_{\nabla e(t)},\cdots, \underbrace{\nabla^{m-1}e_1(t),\cdots,\nabla^{m-1}e_{m_1}(t)}_{\nabla^{m-1}e(t)}]^T \in \mathbb{R}^{(m_1*m)\times 1}$. Manipulating (43), for $g = 1,\cdots,m$, $\varkappa(i+1)$ can be calculated as in (44):

$$\underbrace{\begin{bmatrix} e(i+1) \\ \nabla e(i+1) \\ \vdots \\ \nabla^{m-1}e(i+1) \end{bmatrix}}_{\varkappa(i+1)} = \underbrace{\begin{bmatrix} I_{m_1} & I_{m_1} & \cdots & I_{m_1} \\ 0_{m_1} & I_{m_1} & \cdots & I_{m_1} \\ \vdots & \vdots & \ddots & \vdots \\ 0_{m_1} & 0_{m_1} & \cdots & I_{m_1} \end{bmatrix}}_{E} \underbrace{\begin{bmatrix} e(i) \\ \nabla e(i) \\ \vdots \\ \nabla^{m-1}e(i) \end{bmatrix}}_{\varkappa(i)} - \underbrace{\begin{bmatrix} I_{m_1} \\ I_{m_1} \\ \vdots \\ I_{m_1} \end{bmatrix}}_{\gamma} \times (CA\nabla^m x_m(i) + CB\nabla^m u_m(i)), \quad (44)$$

where $E \in \mathbb{R}^{(m_1*m)\times(m_1*m)}$ is an upper triangular matrix and $\gamma \in \mathbb{R}^{(m_1*m)\times(m_1)}$. Here, I_a denotes an identity matrix of a-order, $0_{m\times n}$ a zero matrix with m rows and n columns and 0_a a zero quadratic matrix of a-order with $a \in \mathbb{N}_+$. Gathering (40a) with (44) leads to the augmented model of

the MIMO system where $A_e \in \mathbb{R}^{(m*m_1+n_1)\times(m*m_1+n_1)}$, $B_e \in \mathbb{R}^{(m*m_1+n_1)\times n_{in}}$, $C_e \in \mathbb{R}^{m_1\times(m*m_1+n_1)}$, $x \in \mathbb{R}^{(m*m_1+n_1)\times 1}$, with x the new augmented state vector while $u(i) = \nabla^m u_m(i)$ and $y(i)$ are the model input and output, respectively.

$$\underbrace{\begin{bmatrix} x(i+1) \\ \nabla^m x_m(i+1) \end{bmatrix}}_{x(i+1)} = \underbrace{\begin{bmatrix} E & -\gamma CA \\ 0_{n_1\times(m*m_1)} & A \end{bmatrix}}_{A_e} \underbrace{\begin{bmatrix} x(i) \\ \nabla^m x_m(i) \end{bmatrix}}_{x(i)} + \underbrace{\begin{bmatrix} -\gamma CB \\ B \end{bmatrix}}_{B_e} \underbrace{\nabla^m u_m(i)}_{u(i)},$$

$$\underbrace{e(i)}_{y(i)} = \underbrace{\begin{bmatrix} I_{m_1} & 0_{m_1\times(m_1*(m-1)+n_1)} \end{bmatrix}}_{C_e} x(i). \tag{45}$$

Note that the characteristic polynomial equation of the augmented model is:

$$\begin{aligned} \rho(z) &= det \begin{bmatrix} (zI_{m_1*m} - E) & +\gamma CA \\ 0_{n_1\times(m*m_1)} & (zI_{n_1} - A) \end{bmatrix} \\ &= (z-1)^{m_1*m} det(zI - A), \end{aligned} \tag{46}$$

where it was used the property that the determinant of an upper triangular block matrix is equal to the product of the determinants of the matrices on the diagonal. Hence, the eigenvalues of the augmented model are the union of the eigenvalues of the plant model and the $m_1 * m$ eigenvalues, z = 1. This means that there are $m_1 * m$ integrators embedded into the augmented design model. Now, it will be proved that m integrators are inserted on each output of the augmented system. Let $L = zI_{n_1} - A$, $\Gamma = zI_{m_1*m} - E$, $\Gamma^{-1} = \begin{bmatrix} Z \\ \Theta \end{bmatrix}$ and $I = \begin{bmatrix} I_{m_1*m} & 0_{(m*m_1)\times n_1} \\ 0_{n_1\times(m*m_1)} & I_{n_1} \end{bmatrix}$, where $Z = [\zeta_1, \zeta_2, \cdots, \zeta_m] \in \mathbb{R}^{m_1\times(m*m_1)}$ is the m_1 first rows of Γ^{-1}, $\zeta \in \mathbb{R}^{m_1\times m_1}$ and $\Theta \in \mathbb{R}^{m_1*(m-1)\times(m*m_1)}$. Regarding (38), (45) and the definitions aforementioned, the transfer functions of the plant and the proposed MIMO model are respectively $G(z) = C(zI_{n_1} - A)^{-1}B = CL^{-1}B$ and $G_p(z) = C_e(zI - A_e)^{-1}B_e$. Remark that $AL^{-1} = (zI_{n_1} - L)L^{-1} = zL^{-1} - I_{n_1}$. Therefore $G_p(z)$ can be calculated as follows:

$$\begin{aligned} G_p(z) &= C_e(zI - \begin{bmatrix} E & -\gamma CA \\ 0_{n_1\times(m*m_1)} & A \end{bmatrix})^{-1}B_e \\ &= \begin{bmatrix} I_{m_1} & 0_{m_1\times(m_1*(m-1))} | & 0_{m_1\times n_1} \end{bmatrix} \\ &\quad \times \begin{bmatrix} \Gamma & \gamma CA \\ 0_{n_1\times(m*m_1)} & L \end{bmatrix}^{-1} \begin{bmatrix} -\gamma CB \\ B \end{bmatrix} \\ &= -\begin{bmatrix} I_{m_1} & 0_{m_1\times(m_1*(m-1))} | & 0_{m_1\times n_1} \end{bmatrix} \\ &\quad \times \begin{bmatrix} \Gamma^{-1} & -\Gamma^{-1}\gamma CAL^{-1} \\ 0_{n_1\times(m*m_1)} & L^{-1} \end{bmatrix} \begin{bmatrix} \gamma CB \\ -B \end{bmatrix} \\ &= -\begin{bmatrix} I_{m_1} & 0_{m_1\times(m_1*(m-1))} \end{bmatrix} \\ &\quad \times \begin{bmatrix} \Gamma^{-1}\gamma CB + \Gamma^{-1}\gamma C(AL^{-1})B \end{bmatrix} \\ &= -\begin{bmatrix} I_{m_1} & 0_{m_1\times(m_1*(m-1))} \end{bmatrix} \\ &\quad \times \Gamma^{-1}\gamma \begin{bmatrix} CB + C(zL^{-1} - I_{n_1})B \end{bmatrix} \\ &= -\begin{bmatrix} I_{m_1} & 0_{m_1\times(m_1*(m-1))} \end{bmatrix} \begin{bmatrix} Z \\ \Theta \end{bmatrix} z\gamma \underbrace{CL^{-1}B}_{G(z)} \\ \therefore G_p(z) &= -Z\gamma zG(z). \end{aligned} \tag{47}$$

As regards $(\Gamma^{-1}\Gamma)^T = I_{m_1*m} = \Gamma^T(\Gamma^{-1})^T = \Gamma^T\begin{bmatrix} Z^T & \Theta^T \end{bmatrix} = \begin{bmatrix} \Gamma^T Z^T & \Gamma^T\Theta^T \end{bmatrix} = I_{m_1*m}$ and $\Gamma^T Z^T \in \mathbb{R}^{(m_1*m)\times m_1}$, hence $\Gamma^T Z^T = \begin{bmatrix} I_{m_1} & 0_{m_1\times(m_1*(m-1))} \end{bmatrix}^T$. Thus:

$$\underbrace{\begin{bmatrix} (z-1)I_{m_1} & 0_{m_1} & \cdots & 0_{m_1} \\ -I_{m_1} & (z-1)I_{m_1} & \cdots & 0_{m_1} \\ \vdots & \vdots & \ddots & \vdots \\ -I_{m_1} & -I_{m_1} & \cdots & (z-1)I_{m_1} \end{bmatrix}}_{\Gamma^T} \underbrace{\begin{bmatrix} \zeta_1 \\ \zeta_2 \\ \vdots \\ \zeta_m \end{bmatrix}}_{Z^T} = \begin{bmatrix} I_{m_1} \\ 0_{m_1} \\ \vdots \\ 0_{m_1} \end{bmatrix}. \tag{48}$$

By [31], one can find $Z\gamma$ when it is applied the following steps: it is straightforward that $\zeta_1 = \frac{I_{m_1}}{z-1}$ and $\zeta_k = \frac{\sum_{j=1}^{k-1}\zeta_j}{z-1}, k = 2, \ldots, m$. By doing $b_1 = \zeta_1$ and $b_k = \sum_{j=1}^{k}\zeta_j$, then $\zeta_k = \frac{b_{k-1}}{z-1}$ and $b_k = \zeta_k + \sum_{j=1}^{k-1}\zeta_j = \zeta_k + b_{k-1}$. Thus:

$$b_k = \frac{b_{k-1}}{z-1} + b_{k-1} = \frac{z}{z-1}b_{k-1},\ b_k = \sum_{j=1}^{k}\zeta_j. \tag{49}$$

It is remarkable that (49) is a geometrical progression where $b_m = b_1(\frac{z}{z-1})^{m-1} = \frac{z^{m-1}}{(z-1)^m}I_{m_1}$ [30]. Also remark that the factor $Z\gamma$ is still necessary, therefore, as regards (44):

$$\begin{aligned} Z\gamma &= \begin{bmatrix} \zeta_1 & \cdots & \zeta_m \end{bmatrix} \begin{bmatrix} I_{m_1} & \cdots & I_{m_1} \end{bmatrix}^T = \sum_{j=1}^{m}\zeta_j \\ &= b_m = \frac{z^{m-1}}{(z-1)^m}I_{m_1}. \end{aligned} \tag{50}$$

Replacing (50) into (47), yields:

$$G_p(z) = -\frac{z^{m-1}}{(z-1)^m}I_{m_1}zG(z) = -(\frac{z}{z-1})^m I_{m_1}G(z) \tag{51}$$

Here, the term $\frac{z}{z-1}$ denotes a discrete integrator. It is noticeable that $G(z) \in \mathbb{R}^{m_1\times n_{in}}$ such that each output transfer function can be written as related to the inputs $U_1, U_2, \ldots, U_{n_{in}}$ in (52):

$$G_{p_k}(z) = -(\frac{z}{z-1})^m \sum_{j=1}^{n_{in}} G_{k,j}(z)U_j(z), \tag{52}$$

where $k = 1, 2, \cdots, m_1$. Thus, (52) asserts that each output has m embedded integrators as desired. According to the IMP, it is required that the plant is controllable with minimal realization, and $G_{k,j}(z)$ has no zero at

$z = 1$. The required number of embedded integrators (m) is defined by the reference degree ($m - 1$). Here, the reactor linearization generated a non-minimal realization plant such that one requirement is not achieved. This highlights the difficulty of controlling high-order nonlinear systems with MIMO. However, even though missing one prerequisite, the improvement of the power steady-state error with GPC type-2 is far more preferable than GPC type-1 for ramp-power tracking and ramp-temperature tracking as it is shown in Section V.

B. OPERATIONAL PRINCIPLE OF THE GPC WITH LAGUERRE FUNCTIONS

Discrete-time Laguerre functions form a set of orthonormal basis in Hilbert space $H_2[0, \infty)$ [32]. Considering stable the augmented system in (45), it is straightforward that $u(k)$ is square-summable on $0 \leq k \leq \infty$, i.e. $\sum_{k=0}^{\infty} u^2(k) < \infty$. Thus, $u(k)$ fulfills the necessary requirement to be spanned in $H_2[0, \infty)$ space such that orthonormal Laguerre functions were chosen regarding its simplicity and good resolution in slow systems. While Fourier spectrum is notorious in expansion of periodic signals, Laguerre functions have gained wide application in signal approximation on power systems [33].

The Laguerre network is determined by its pole (a) and the number of functions (N), with $0 \leq a < 1$ and $N \in \mathbb{N}^*$. Here, the slight error of the $u(k)$ expansion with a small value of N highlights the applicability of Laguerre functions in this work. Thus, z-transform of the discrete-time Laguerre functions can be expressed as [34] and [35]:

$$\Gamma_N(z) = \frac{\sqrt{1-a^2}}{1-az^{-1}}\left(\frac{z^{-1}-a}{1-az^{-1}}\right)^{N-1}, \tag{53}$$

Remark that (53) can be written as a recursive form:

$$\begin{aligned}\Gamma_k(z) &= \Gamma_{k-1}(z)\left(\frac{z^{-1}-a}{1-az^{-1}}\right),\\ \Gamma_1(z) &= \frac{\sqrt{1-a^2}}{1-az^{-1}}.\end{aligned} \tag{54}$$

After doing the inverse discrete-time transform of (53), the set of discrete-time Laguerre functions $L(k)$, at sample instant k, satisfies the following difference equation:

$$L(k+1) = A_l L(k), \tag{55}$$

where A_l is a $(N \times N)$ inferior triangular Toeplitz matrix and a function of parameters a and $\beta = (1 - a^2)$ [36]. $L(k)$ has initial conditions given by:

$$L(0)^T = \sqrt{\beta}\left[1 \; -a \; a^2 \; \ldots \; (-1)^{N-1}a^{N-1}\right], \tag{56}$$

Using Laguerre functions to find the fittest expansion of the control trajectory ($u(k_i + k)$) (45) of a stable dynamic system at an arbitrary future sample instant k from k_i [37], it can be written (57):

$$u(k_i + k) = \sum_{j=1}^{N} c_j(k) l_j(k) = L(k)^T \eta, \tag{57}$$

where the parameter vector $\eta^T = \left[c_1 \; c_2 \; \ldots \; c_N\right]$ comprises N Laguerre coefficients and $L(k)^T$ is the transposed Laguerre function vector at a future sampling k. Here, the control horizon used at standard GPC has vanished due to the approximation feature of the Laguerre expansion. However, the number of terms N is used to fit u behavior with the parameter a.

Based on the aforementioned definitions of Laguerre functions in SISO systems, one can extend to MIMO with full flexibility in the choice of a and N on each dimension [38]. Let $u(k_i) = \left[u_1(k_i) \; u_2(k_i) \; \cdots \; u_{n_{in}}(k_i)\right]^T$ and the input matrix be partitioned to $B_e = \left[B_{e_1} \; B_{e_2} \; \cdots \; B_{e_{n_{in}}}\right]$, hence (57) can be expressed as the *ith* ($1 \leq i \leq n_{in}$) control signal by choosing a pole a_i and order N_i, where a_i and N_i are selected for this particular input, such that:

$$u_i(k_i + k) = L_i(k)^T \eta_i, \tag{58}$$

where η_i and $L_i(k)$ are the Laguerre network description of the *ith* control. Based on the state-space (A_e, B_e, C_e) initialized at sample k_i, from (45), the future state variables are calculated sequentially using the set of future control parameters until the sampling n.

$$\begin{aligned}x(k_i+1) &= A_e x(k_i) + B_e u(k_i),\\ x(k_i+2) &= A_e^2 x(k_i) + A_e B_e u(k_i) + B_e u(k_i+1),\\ &\vdots\\ x(k_i+n) &= A_e^n x(k_i) + \sum_{i=0}^{n-1} A_e^{n-i-1} B_e u(k_i+i).\end{aligned} \tag{59}$$

Notice that, from (45), the predicted output variable from sample k_i to n is found multiplying the future state variables (59) by C_e, therefore:

$$y(k_i+n) = C_e A_e^n x(k_i) + \sum_{i=0}^{n-1} C_e A_e^{n-i-1} B_e u(k_i+i). \tag{60}$$

Thus, applying (58) in (59) and (60), the prediction of the future state variable $x(k_i + n)$ and the prediction of the plant output $y(k_i + n)$, at sampling instant n, become (61a) and (61b).

$$\begin{aligned}x(k_i+n) &= A_e^n x(k_i) + \sum_{i=0}^{n-1} A_e^{n-i-1} B_e L(i)^T \eta\\ &= A_e^n x(k_i) + \sum_{i=0}^{n-1} A_e^{n-i-1}[B_{e_1} L_1(i)^T\\ &\quad \cdots B_{e_{n_{in}}} L_{n_{in}}(i)^T]\eta\\ &= A_e^n x(k_i) + \varphi(n)^T \eta,\end{aligned} \tag{61a}$$

$$\begin{aligned}y(k_i+n) &= C_e A_e^n x(k_i) + \sum_{i=0}^{n-1} C_e A_e^{n-i-1} B_e L(i)^T \eta\\ &= C_e A_e^n x(k_i) + \sum_{i=0}^{n-1} C_e A_e^{n-i-1}[B_{e_1} L_1(i)^T\end{aligned}$$

$$\cdots B_{e_{n_{in}}} L_{n_{in}}(i)^T]\eta = C_e A_e^n x(k_i) + C_e \varphi(n)^T \eta, \quad (61b)$$

where the parameter vector η^T and the auxiliary matrix $\varphi(n)^T$ consist of the individual coefficient vectors given by $\eta^T = [\eta_1^T \ \eta_2^T \ \cdots \ \eta_{n_{in}}^T]$ and $\varphi(n)^T = \sum_{i=0}^{n-1} A_e^{n-i-1} [B_{e_1} L_1(i)^T \ \cdots \ B_{e_{n_{in}}} L_{n_{in}}(i)^T]$.

From [38], by defining Y (vector of predicted model outputs), U (vector of future control actions), N_p (prediction horizon) and N_c (control horizon), it can be noted that:

$$Y = \left[y(k_i+1) \ y(k_i+2) \ \cdots \ y(k_i+N_p)\right]^T, \quad (62a)$$

$$U = \left[u(k_i) \ u(k_i+1) \ \cdots \ u(k_i+N_c-1)\right]^T, \quad (62b)$$

The objective of GPC is to find an optimal U that minimize the cost function J that measures the control performance. Let $R_s \in \mathbb{R}^{N_p \times m_1}$ be the future set-point vector for Y in (62a). It is assumed that R_s is constant over the prediction horizon. In [38], the cost function is defined as

$$J = (R_s - Y)^T (R_s - Y) + U^T R^* U, \ R^* = r_w I_{N_p}, \quad (63)$$

with $r_w > 0$. The vector of predicted model outputs Y in (62a) is composed by the predicted errors. It is worth mentioning that the weight importance of r_w in (63) is such that its reduction yields in a faster control actuation and faster closed-loop dynamics, however, its robustness is compromised and wider constraints are demanded. As the desired value of an error is zero, the set-point vector R_s for Y is a set of zeros, i.e., $R_s = 0_{N_p \times m_1}$. Noting that Y and U are in a vector form and using (58) and appendix B, the cost function (63) becomes:

$$J = \sum_{n=1}^{N_p} y(k_i+n)^T y(k_i+n) + \eta^T R_L \eta, \quad (64)$$

where $R_L \in \mathbb{R}^{\sum N_i \times \sum N_i}$ and N_p is the prediction horizon, big enought ($N_p \to \infty$) to validate the orthonomal property of Laguerre functions (65)

$$\sum_{n=0}^{\infty} l_i(n) l_j(n) = \begin{cases} 1, & if \ i = j \\ 0, & if \ i \neq j \end{cases}, \quad (65)$$

As regards (61b) in (64) and defining $Q = C_e^T C_e$ (positive semidefinite matrix), one can note that:

$$J = \sum_{n=1}^{N_p} x(k_i+n)^T Q x(k_i+n) + \eta^T R_L \eta. \quad (66)$$

This paper researches a fitter model to create a accurate system. In doing so, one must be aware of the problem of numerical ill-conditioning with respect to a large prediction horizon. Due to the high dimension of the ERB-II system, the Q and R_L matrices are modified to ensure numerical stability against numerical ill-condition and created a λ-circle in which all the closed-loop poles of the predictive control system are to reside. By doing so, the matrices Q and R_L become Q_α and R_α by choosing a pair (α, λ), with $\alpha \geq 1$ and $0 < \lambda \leq 1$, and solving the steady-state Riccati equation (67a) to find P_∞ [38].

$$\frac{A^T}{\lambda}[P_\infty - P_\infty \frac{B}{\lambda}(R_L + \frac{B^T P_\infty B}{\lambda^2})^{-1} \frac{B^T}{\lambda}]\frac{A}{\lambda} + Q - P_\infty = 0, \quad (67a)$$

$$\gamma = \frac{\lambda}{\alpha}, \quad (67b)$$

$$Q_\alpha = \gamma^2 Q + (1-\gamma^2) P_\infty, \quad (67c)$$

$$R_\alpha = \gamma^2 R_L. \quad (67d)$$

Finally, (66) becomes:

$$J = \sum_{n=1}^{N_p} x(k_i+n)^T Q_\alpha x(k_i+n) + \eta^T R_\alpha \eta. \quad (68)$$

Replacing (61a) in (68), yields:

$$J = \sum_{n=1}^{N_p} (A_e^n x(k_i) + \varphi(n)^T \eta)^T Q_\alpha (A_e^n x(k_i) + \varphi(n)^T \eta) + \eta^T R_\alpha \eta$$

$$J = \sum_{n=1}^{N_p} [x(k_i)^T (A_e^T)^n Q_\alpha A_e^n x(k_i) + x(k_i)^T (A_e^T)^n Q_\alpha \varphi(n)^T \eta + \eta^T \varphi(n) Q_\alpha A_e^n x(k_i) + \eta^T \varphi(n) Q_\alpha \varphi(n)^T \eta] + \eta^T R_\alpha \eta. \quad (69)$$

Noting that $\eta^T \varphi(n) Q_\alpha A_e^n x(k_i)$ is a number, i.e., $(\eta^T \varphi(n) Q_\alpha A_e^n x(k_i))^T = x(k_i)^T (A_e^T)^n Q_\alpha \varphi(n)^T \eta$, hence (69) can be written as:

$$J = \eta^T (\sum_{n=1}^{N_p} \varphi(n) Q_\alpha \varphi(n)^T + R_\alpha)\eta + 2\eta^T (\sum_{n=1}^{N_p} \varphi(n) Q_\alpha A_e^n) x(k_i) + \sum_{n=1}^{N_p} x(k_i)^T (A_e^T)^n Q_\alpha A_e^n x(k_i). \quad (70)$$

Without constraints, the partial derivative of the cost function $\frac{\partial J}{\partial \eta}$ is performed to find the minimum of (70).

$$\frac{\partial J}{\partial \eta} = 2(\sum_{n=1}^{Np} \varphi(n) Q_\alpha \varphi(n)^T + R_\alpha)\eta + 2(\sum_{n=1}^{Np} \varphi(n) Q_\alpha A_e^n) x(k_i). \quad (71)$$

For simplicity, it is defined that:

$$\Omega = \sum_{n=1}^{Np} \varphi(n) Q_\alpha \varphi(n)^T + R_\alpha. \quad (72a)$$

$$\Psi = \sum_{n=1}^{Np} \varphi(n) Q_\alpha A_e^n. \quad (72b)$$

Thus, assuming that Ω^{-1} exists when $\frac{\partial J}{\partial \eta} = 0$, the optimal solution of the parameter matrix η is:

$$\eta = -\Omega^{-1}\Psi x(k_i). \tag{73}$$

Upon obtaining the optimal parameter matrix η, the receding horizon control law for MIMO systems with Laguerre functions is obtained by:

$$u(k_i) = \begin{bmatrix} L_1(0)^T & 0_2^T & \cdots & 0_{n_{in}}^T \\ 0_1^T & L_2(0)^T & \cdots & 0_{n_{in}}^T \\ \vdots & \vdots & \ddots & \vdots \\ 0_1^T & 0_2^T & \cdots & L_{n_{in}}(0)^T \end{bmatrix} \eta, \tag{74}$$

where $0_k^T, k = 1, 2, \cdots n_{in}$, represents a zero block row vector with identical dimension to $L_k(0)^T$, i.e., N_k.

The most important constraints are associated with the control signals, be it the amplitude of the control or the difference of the control. The less important constraints are the output constraints, owing to their narrow correlation with an accurate linearized system [38]. By assuming that hierarchy, at each iteration of the receding horizon, after the calculation of parameter matrix η leading to the optimal control variable $u(k_i)$, the algorithm integrates m times $u(k_i)$ to get $u_m(k_i)$ then compares the difference of the control variable with its constraints. If the difference of the control variable is higher than its maximum constraint, its value becomes this maximum value, in the same way, if the difference of the control variable is lower than its minimum constraint, its value becomes this minimum value. By doing that, the algorithm updates the control variable and whether its value is higher than its maximum constraint, the difference of the control variable becomes $u_{max} - u_m(k_i - 1)$ and the control variable becomes u_{max}, in the same way, if the control variable value is lower than its minimum constraint, the difference of the control variable becomes $u_{min} - u_m(k_i - 1)$ and the control variable becomes u_{min}. No output variable constraints were used in this paper.

IV. PROPOSED CONTROL APPROACH

The main objective of this paper is to design a GPC controller that controls three measured outputs as regards three manipulated variables added with three measured disturbances and one unmeasured disturbance for SFR. The literature describes physical constraints concerning the maximum rate of reactivity insertion and the maximum rate of coolant temperature difference across the core, i.e. the maximum rate of the temperature between core and tank (nodes 26 and 37). Those constraints are $\Delta reactivity/\Delta t \leq 1\ cent/sec$ and $\Delta T_{core}/\Delta t < 2\ F/min$ [4]. For a correct functioning of the reactor in any power operation, the secondary flow rate of sodium need to be controlled to absorb all heat in excess to maintain the tank temperature ($y(3)$) at a constant temperature of 669.72^oF [4].

In order to fulfill the temperature constraint, it is required to control the coolant temperature difference across the core

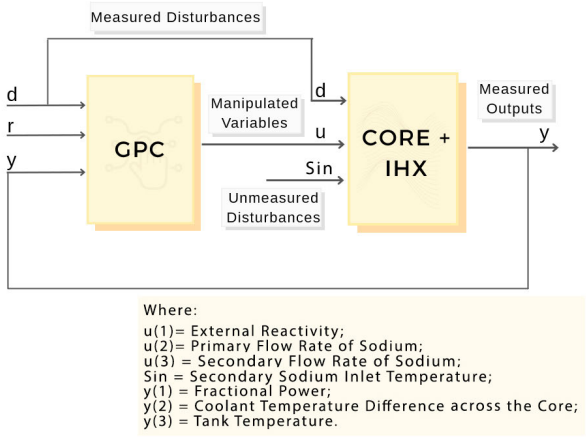

FIGURE 3. Closed-loop EBR-II Core + IHX controled by the proposed GPC.

($y(2)$) as related to its initial operating point of 183.07^oF. For this purpose, the primary flow rate of sodium was chosen to stabilize the core temperature with the power variation. Figure 3 shows the overview of the closed-loop EBR-II Core + IHX controlled by the proposed GPC. The references to be tracking are fractional power, the coolant temperature difference across the core and tank temperature, therefore they were designed with initial value $r_0 = [1; 183.07; 699.72]$ for 100% power operation.

According to the small variations in reactivity defined by the physical constraint of the reactor, the input weight of $u(1)$ must be the smallest possible to generate the fastest control. Accordingly, the input weights of $u(2)$ and $u(3)$ should be greater than $u(1)$ to ensure the reactor safety as related to the constraint on the coolant temperature difference rate across the core. In general, the augmented matrices of the proposed method create huge Ω and Φ matrices, therefore it can be noted a large size of the condition number for the closed-loop system. This requires a careful choice of setup parameters for the initialization of the GPC because it is sought in this paper to avoid ill-conditioned problems with a good trade-off in terms of the algorithm convergence. However, small input weights drive to a loss in robustness and an increase in the Hessian matrix condition number. Moreover, the exponential factor, responsible to decrease the Hessian matrix condition number, may compromise the performance of the closed-loop system if tuned with high value. The number of Laguerre functions in each manipulated variable must be capable to identify the augmented manipulated variable with a reduced number and without losing performance. Thus, following the assumptions aforementioned, by a trial and error fashion, TABLE 2 presents the setup parameters of the unconstrained GPC type 1 and 2 with similar Hessian matrix condition number and identical input weights.

TABLE 3 presents the setup constraints of GPC as related to u and ∇u. The constraint from -7 to 7 cents on the reactivity agrees with the robustness aim related to: (a) rejecting external reactivity disturbance up to -1 cents without violating

TABLE 2. Setup parameters of the GPC.

Parameter Name	GPC type-1	GPC type-2
R_L	$[10^{-6}, 0, 0; 0, 10^{-3}, 0; 0, 0, 10^{-3}]$	$[10^{-6}, 0, 0; 0, 10^{-3}, 0; 0, 0, 10^{-3}]$
a	[0.4,0.4,0.4]	[0.4,0.4,0.4]
N	[2;2;2]	[2;2;2]
N_p	20	20
λ	1	1
α	1.3	1.57
$\kappa(\Omega)$	582.24	590.26

TABLE 3. Setup constraints of GPC.

Variable	Minimum value	Maximum value
u	$[-7; 4500; 2945]$	$[7; 13500; 8835]$
∇u	$[-1; -\infty; -\infty]$	$[1; \infty; \infty]$

the temperature constraint; and (b) ramp-reference tracking. It is also noticeable that the control variable rate was calculated per second so the values in TABLE 3 satisfy $\Delta reactivity/\Delta t \leq 1\ cent/sec$. As regards the primary and secondary sodium flow rates, the startup values for the full power operation are 9000 gallons per minute (gpm) and 5890 gpm [4], respectively. Thus, the initial values of the control variables utilized were $u_0 = [0; 9000; 5890]$. The acting control handles automatically the sodium pumps in order to control the operation in a flux range around $\pm 50\%$ of the startup. This approach is required due to the disturbance injection in the secondary sodium inlet temperature and the ramp-reference tracking. The unconstrained feature of the flow rate derivative has a reasonable meaning, because the pump control valves can drop or increase the flow rate for the entire range in one second. Note that the secondary sodium inlet temperature (unmeasured disturbance) is set as 588^oF [4].

According to the proposed MIMO augmented state-space matrices (45) generated with the digital state-space matrices of the reactor and the number of required embedded integrators, the parameters in TABLE 2 were performed with the "dlqr" and "dmpc" functions of MATLAB to attain the matrices Ω and Ψ [38]. Based on MATLAB/Simulink environment, the algorithm 1 was built with the following blocks: MATLAB function and data store memory. Note that the size of global matrices was created regarding the choice of m. Finally, the "lagd" function was utilized to calculate the Laguerre coefficients according to a and N [38] while the binomial coefficient is $C_m^i = \dfrac{m!}{i!(m-i)!}$.

V. SIMULATIONS AND RESULTS

In this section, the step perturbations and the reference variations were carried out while the closed-loop systems operated in full-power mode after 8000 seconds from the startup. In order to perform the coolant temperature difference rate across the core with the controllers, $\Delta T_{core-m}/\Delta t = (60\nabla y(2))/(60T_s) = 60\nabla y(2)^oF/min$. Remind that the tank temperature must be unchanged, independently the reactor's operating point.

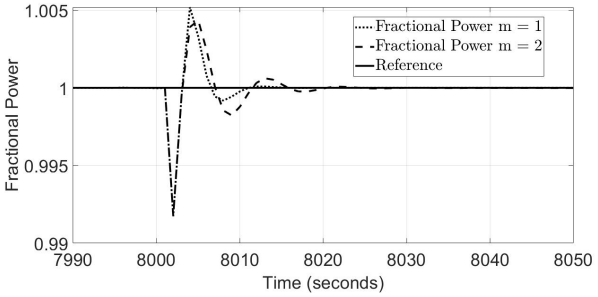

FIGURE 4. First simulation: fractional power.

TABLE 4. MSE - first simulation.

Output	m = 2	m = 1
Fractional power	$2.33 \cdot 10^{-8}$	$2.17 \cdot 10^{-8}$
Coolant temperature difference	$2.62 \cdot 10^{-6}$	$2.27 \cdot 10^{-6}$
Tank temperature	$9.91 \cdot 10^{-11}$	$2.15 \cdot 10^{-10}$

A. DISTURBANCE INJECTION ANALYSIS

Simulations were made to compare step perturbations in external reactivity and secondary sodium inlet temperature. The reactivity perturbation is a key process for the measurement of the total delayed neutron fraction [39]. Meanwhile, the disturbance in the secondary sodium inlet temperature emerges when it is implemented the coupling of primary system model to the steam generator [4].

Figures 4 and 5 present the fractional power and the coolant temperature difference across the core of each controller in comparison with their references for the -1 cent reactivity perturbation. TABLE 4 displays the MSE for this first simulation. The absolute maximum rate of the coolant temperature difference across the core agrees with the reactor safety, because $\Delta T_{core-1}/\Delta t \leq 1.776^oF/min$ and $\Delta T_{core-2}/\Delta t \leq 1.796^oF/min$. Figures 6 and 7 show the fractional power and the coolant temperature difference across the core of each controller in comparison with their references for the 10^oF perturbation in the secondary sodium inlet temperature. TABLE 5 displays the MSE for this second simulation. The absolute maximum rate of the coolant temperature difference across the core agrees with the reactor safety, because $\Delta T_{core-1}/\Delta t \leq 0.1444^oF/min$ and $\Delta T_{core-2}/\Delta t \leq 0.1023^oF/min$.

Algorithm 1 GPC Type-m Algorithm

function MV = GPC_SFR(y(k), r(k), d(k))
Require: u_m, x_m, e, δx as global variables;
Require: A_d, B_d, C_d matrices;
Require: N, $\Omega^{-1}\Psi$, a, m, u_{max}, u_{min}, ∇u_{max}, ∇u_{min};
$[m_1, n_1] \leftarrow size(C_d)$;
$[n_1, n_{in}] \leftarrow size(B_d)$;
for $i = m - 1$ to $i = 1$ **do**
  $e(k - i) \leftarrow e(k - (i - 1))$;
end for
$e(k) \leftarrow r(k) - y(k)$;
▷ Error updating
$\varkappa(k) \leftarrow zeros$;
for $i = 0$ to $i = m - 1$ **do**
  for $j = 0$ to $j = i$ **do**
    $\varkappa(m_1 * i + 1 : m_1 * (i + 1), k) \leftarrow \varkappa(m_1 * i + 1 : m_1 * (i + 1), k) + e(j + 1) * C_i^j * (-1)^j$;
  end for
end for
▷ $\varkappa$ updating
for $i = m$ to $i = 1$ **do**
  $\delta x(k - i) \leftarrow \delta x(k - (i - 1))$;
end for
$\delta x(k) \leftarrow x_m(k)$;
▷ State-variable updating
$\nabla^m x_m(k) \leftarrow \sum_{i=0}^{m} C_m^i * (-1)^i * \delta x(k - i)$;
$x(k) \leftarrow [\varkappa(k); \nabla^m x_m(k)]$;
▷ Augmented state-variable updating
$L_0 \leftarrow lagd(a(1), N(1))$;
$L_m(1, 1 : N(1)) \leftarrow L_0^T$;
if $n_{in} > 1$ **then**
  $aux \leftarrow 1$;
  for $v = 2$ to $v = n_{in}$ **do**
    $L_0 \leftarrow lagd(a(v), N(v))$;
    $aux \leftarrow N(v - 1) + aux$;
    $aux2 \leftarrow N(v) + aux - 1$;
    $L_m(v, aux : aux2) \leftarrow L_0^T$;
  end for
end if
▷ Laguerre coefficients
$\eta(k) \leftarrow -\Omega^{-1}\Psi * x(k)$;
$u(k) \leftarrow L_m * \eta(k)$;
$u_p \leftarrow u_m(k)$;
$u_m(k) \leftarrow u(k) - \sum_{i=1}^{m} C_m^i * (-1)^i * u_m(k - i)$;
$\nabla u_m(k) \leftarrow u_m(k) - u_p$;
Hard limit constraint evaluation of $\nabla u_m(k)$;
$u_m(k) \leftarrow u_p + \nabla u_m(k)$;
Hard limit constraint evaluation of $u_m(k)$;
$x_m(k) \leftarrow A_d * x_m(k) + B_d * (u_m(k) + d(k))$;
▷ State-variable updating
for $i = m$ to $i = 1$ **do**
  $u_m(k - i) \leftarrow u_m(k - (i - 1))$;
end for
▷ Manipulated variables updating.
$MV \leftarrow u_m(k)$;
end function

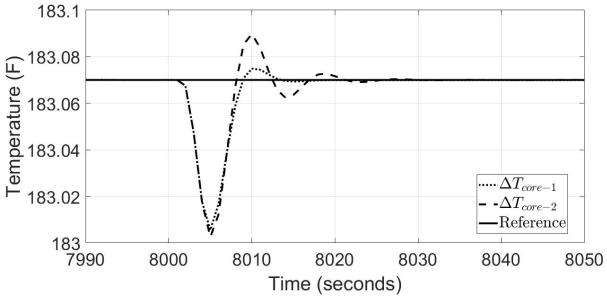

FIGURE 5. First simulation: coolant temperature difference across the core.

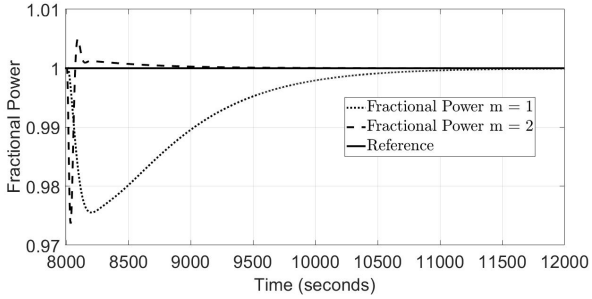

FIGURE 6. Second simulation: fractional power.

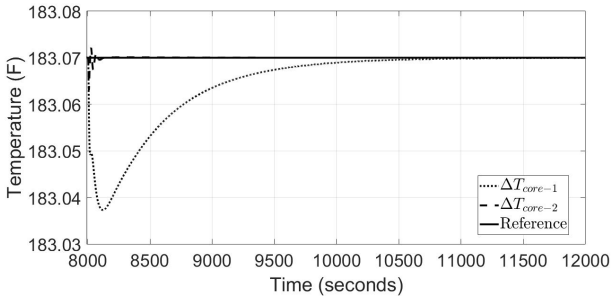

FIGURE 7. Second simulation: coolant temperature difference across the core.

TABLE 5. MSE - second simulation.

Output	m = 2	m = 1
Fractional power	$3.97 \cdot 10^{-6}$	$7.22 \cdot 10^{-5}$
Coolant temperature difference	$8.37 \cdot 10^{-8}$	$7.94 \cdot 10^{-5}$
Tank temperature	$6.85 \cdot 10^{-5}$	0.014

B. TEMPERATURE-TRACKING ANALYSIS

In order to simulate the power behavior with the temperature modification, the reference of the coolant temperature difference across the core was established as follows:

- From 8000 to 9200 seconds: the temperature changes as a linear ramp from 183.07^oF to 223.07^oF with a slope of $2^oF/min$;
- From 9200 to 11700 seconds: the temperature remains at 223.07^oF.
- From 11700 to 13000 seconds: the temperature changes as a linar ramp from 223.07^oF to 183.07^oF with a slope of $-2^oF/min$;

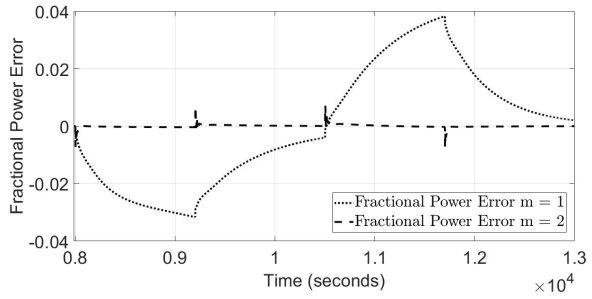

FIGURE 8. Third simulation: fractional power error.

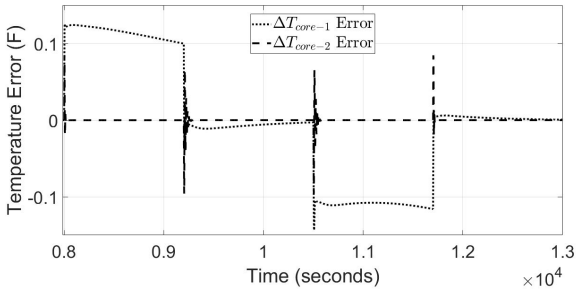

FIGURE 9. Third simulation: coolant temperature difference error across the core.

TABLE 6. MSE - third simulation.

Output	m = 2	m = 1
Fractional power	$3.08 \cdot 10^{-7}$	$4.23 \cdot 10^{-4}$
Coolant temperature difference	$3.23 \cdot 10^{-5}$	$6.1 \cdot 10^{-3}$
Tank temperature	$1.64 \cdot 10^{-6}$	$5.2 \cdot 10^{-3}$

Figures 8 and 9 exhibit the fractional power error and the coolant temperature difference error across the core of each controller for the ramp-temperature tracking. The fractional power reference remains at its full-power operation. Moreover, the temperature slope of the simulation agrees with the absolute maximum rate of coolant temperature difference across the core. TABLE 6 displays the MSE for this third simulation. Remark that the GPC-SFR type-1 cannot achieve the zero steady-state error for the ramp-temperature tracking while the fractional power missed the operating point.

C. LOAD-TRACKING ANALYSIS

In order to simulate the load-following process of the SFR, the references of fractional power and coolant temperature difference across the core were established as follows:

- From 8000 to 11000 seconds: the fractional power changes as a linear ramp from 100% FP to 60% FP with a slope of -0.8% FP/min. Meanwhile, the temperature changes as a linear ramp from 183.07^oF to 160.57^oF with a slope of $-0.45^oF/min$;
- From 11000 to 14000 seconds: the fractional power and the temperature remain at 60% FP and 160.57^oF, respectively.

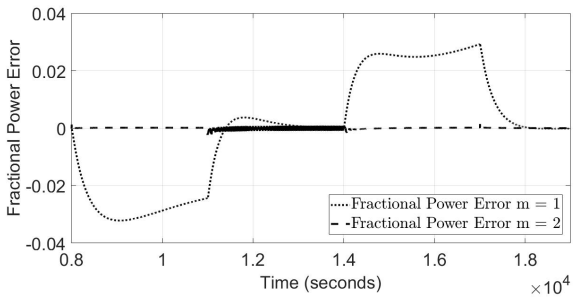

FIGURE 10. Fourth simulation: fractional power error.

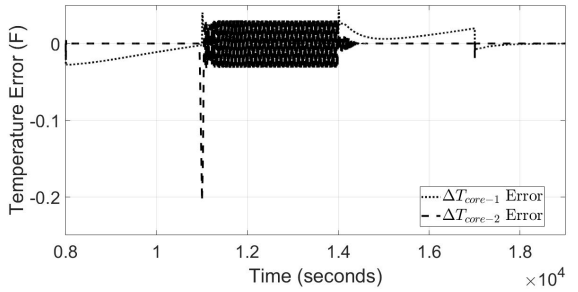

FIGURE 11. Fourth simulation: coolant temperature difference error across the core.

TABLE 7. MSE - fourth simulation.

Output	m = 2	m = 1
Fractional power	$1.61 \cdot 10^{-7}$	$3.93 \cdot 10^{-4}$
Coolant temperature difference	$2.7 \cdot 10^{-4}$	$1.59 \cdot 10^{-4}$
Tank temperature	$8.66 \cdot 10^{-7}$	$1.05 \cdot 10^{-2}$

- From 14000 to 17000 seconds: the fractional power changes as a linear ramp from 60% FP to 100% FP with a slope of 0.8% FP/min. Meanwhile, the temperature changes as a linear ramp from 160.57^oF to 183.07^oF with a slope of $0.45^oF/min$;

Figures 10 and 11 present the fractional power error and the coolant temperature error across the core of each controller for the load-following process. TABLE 7 displays the MSE for this fourth simulation. A small oscillatory error for the GPC-SFR type-2 emerges owing to the external reactivity constraint (-7 cent). The deviation error is 0.17% of the 60% FP. However, this oscillatory behavior has no interference in the reactor safety; therefore, the SFR can operate at 60% FP. The absolute maximum rate of coolant temperature difference across the core agrees with the reactor safety, because $\Delta T_{core-1}/\Delta t \leq 0.5666^oF/min$ and $\Delta T_{core-2}/\Delta t \leq 0.9056^oF/min$. Finally, both controllers can handle the power reduction; however, the GPC-SFR type-2 demonstrated faster performance than the GPC type-1 and zero steady-state error in the ramp-load tracking.

D. STABILITY SIMULATION

The SFR fuel alloy composition contains mid-enriched uranium at the beginning (48.4%) [4]. During the burn-up

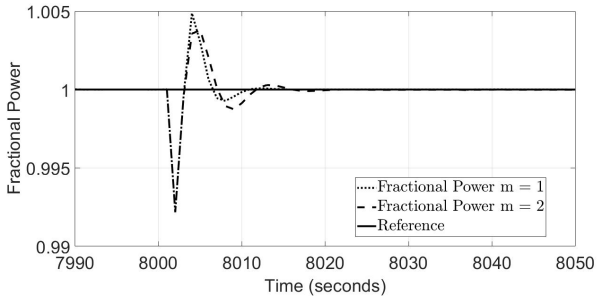

FIGURE 12. Fifth simulation: fractional power.

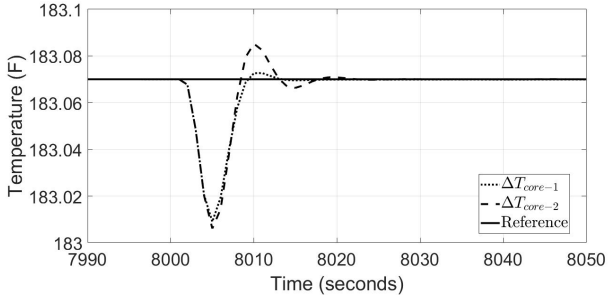

FIGURE 13. Fifth simulation: coolant temperature difference across the core.

TABLE 8. MSE - fifth simulation.

Output	m = 2	m = 1
Fractional power	$1.93 \cdot 10^{-8}$	$1.92 \cdot 10^{-8}$
Coolant temperature difference	$2.35 \cdot 10^{-6}$	$2.05 \cdot 10^{-6}$
Tank temperature	$8.34 \cdot 10^{-11}$	$2.19 \cdot 10^{-10}$

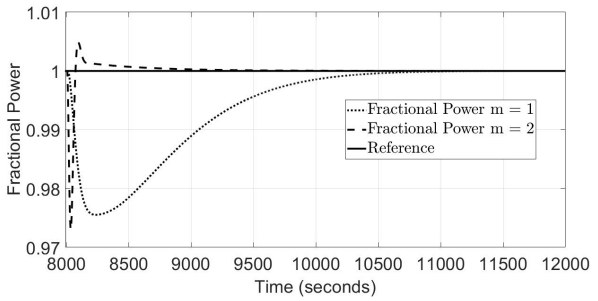

FIGURE 14. Sixth simulation: fractional power.

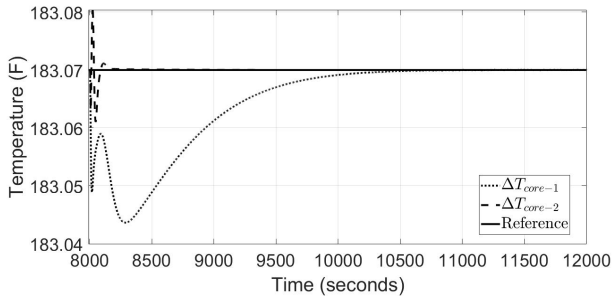

FIGURE 15. Sixth simulation: coolant temperature difference across the core.

TABLE 9. MSE - sixth simulation.

Output	m = 2	m = 1
Fractional power	$4.17 \cdot 10^{-6}$	$7.87 \cdot 10^{-5}$
Coolant temperature difference	$5.83 \cdot 10^{-7}$	$7.13 \cdot 10^{-5}$
Tank temperature	$7.03 \cdot 10^{-5}$	$1.64 \cdot 10^{-2}$

process, plutonium and other elements are built up, reducing the total delayed neutron fraction (β_T). Furthermore, the uncertainty in the measure of β_T is a concurrent problem for the reactor design [40]. According to the nonlinear equations (1) and (2), the operating point is highly modified with the β_T reduction. Thus, the GPC-SFR must guarantee robustness against perturbations at the 100% FP with a reduced β_T.

In order to perform a reliable simulation, the nonlinear model was updated with a 5% reduction in β_T. Figures 12 and 13 present the fractional power and the coolant temperature difference across the core of each controller in comparison with their references for the -1 cent reactivity perturbation. TABLE 8 displays the MSE for this fifth simulation. The absolute maximum rate of the coolant temperature difference across the core agrees with the reactor safety, because $\Delta T_{core-1}/\Delta t \leq 1.67^oF/min$ and $\Delta T_{core-2}/\Delta t \leq 1.69^oF/min$. Figures 14 and 15 show the fractional power and the coolant temperature difference across the core of each controller in comparison with their references for the 10^oF perturbation in the secondary sodium inlet temperature. TABLE 9 displays the MSE for this sixth simulation. The absolute maximum rate of the coolant temperature difference across the core agrees for the reactor safety with $\Delta T_{core-1}/\Delta t \leq 0.1486^oF/min$ and $\Delta T_{core-2}/\Delta t \leq 0.1086^oF/min$.

VI. CONCLUDING REMARKS

This paper has presented a novel MIMO GPC type-m based on orthonormal Laguerre functions with input constraints for the primary system of a prototypical SFR (core and IHX) in MATLAB/Simulink. The fractional power, the coolant temperature difference across the core and the tank temperature are regulated through the control of reactivity and sodium flow rates. The novelty of this paper is addressed to the zero steady-state error for ramp-temperature tracking and ramp-load tracking with $m = 2$ with a simple algorithm 1. Constraints on the primary sodium flow rate, secondary flow rate and external reactivity were applied. For a fair comparison, a GPC type-1 was designed with similar proposed parameters. To attain the reactor safety conditions, the coolant temperature difference rate across the core agreed with the maximum allowable of $2^oF/min$ for the following simulations: (a) step perturbations on reactivity and secondary sodium inlet temperature; (b) temperature-tracking analysis; (c) load-tracking analysis; and (d) simulation with uncertainty in reactor design. The GPC-SFR type-2 demonstrates faster performance than the GPC-SFR type-1 in the aforementioned scenarios. For the assigned MSE, the evaluation of TABLES 4 - 9 prove the superiority of the GPC type-2 in 13 of 18 measurements. Finally, the GPC-SFR displays appropriate robustness with regard to the β_T uncertainty during the burn-up process.

APPENDIX A: NON-ZERO ENTRY ELEMENTS OF THE SFR's STATE-SPACE MATRICES

A. MATRIX A

a(1,1) = -0.08	a(1,31) = 46954.8	a(2,2) = -813.38	a(2,13) = 391.46	a(2,24) = 421.92	a(3,3) = -1.3
a(3,4) = 1.3	a(3,31) = 4.59	a(4,3) = 2.62	a(4,4) = -21.49	a(4,37) = 18.87	a(5,3) = 2.62
a(5,4) = 16.25	a(5,5) = -18.87	a(6,6) = -0.08	a(6,7) = 0.08	a(6,31) = 130.02	a(7,6) = 0.17
a(7,7) = -19.04	a(7,33) = 18.87	a(8,6) = 0.17	a(8,7) = 18.7	a(8,8) = -18.87	a(9,9) = -0.08
a(9,10) = 0.08	a(9,31) = 23.04	a(10,9) = 2.25	a(10,10) = -9.65	a(10,37) = 7.4	a(11,9) = 2.25
a(11,10) = 5.16	a(11,11) = -7.4	a(12,12) = -0.01	a(12,14) = 0.01	a(12,31) = 7.25	a(13,2) = 59.66
a(13,13) = -93.29	a(13,32) = 33.64	a(14,12) = 0.07	a(14,14) = -1.9	a(14,35) = 1.84	a(15,12) = 0.07
a(15,14) = 1.77	a(15,15) = -1.84	a(16,8) = 0.12	a(16,11) = 0.03	a(16,15) = 0.02	a(16,16) = -0.17
a(17,16) = 0.65	a(17,17) = -0.65	a(18,17) = 0.52	a(18,18) = -0.52	a(19,18) = 0.53	a(19,19) = -0.76
a(19,21) = 0.22	a(20,19) = 0.31	a(20,20) = -0.55	a(20,21) = 0.22	a(21,19) = 0.3	a(21,21) = -0.66
a(21,23) = 0.36	a(22,21) = 1.15	a(22,22) = -1.4	a(22,23) = 0.34	a(23,21) = 1.15	a(23,23) = -2.46
a(23,28) = 1.4	a(24,2) = 24.61	a(24,24) = -24.61	a(24,31) = 1168.94	a(25,20) = 0.53	a(25,25) = -0.76
a(25,27) = 0.22	a(26,25) = 0.31	a(26,26) = -0.55	a(26,27) =0.22	a(27,25) =0.3	a(27,27) =-0.66
a(27,29) =0.36	a(28,27) =1.15	a(28,28) =-1.4	a(28,29) =0.34	a(29,27) =1.15	a(29,29) =-2.46
a(30,26) = 0.002	a(30,30) =-0.002	a(31,11) =0.08	a(31,4) =-0.09	a(31,5) =-0.09	a(31,7) =-0.09
a(31,8) =-0.09	a(31,10) =-0.38	a(31,11) =-0.38	a(31,13) =-39.76	a(31,24) =-9.82	a(31,31) =-46954.8
a(31,32) =-13.28	a(31,33) =-13.28	a(32,5) =26.67	a(32,13) =26.85	a(32,32) =-53.51	a(33,13) =26.85
a(33,32) =-0.18	a(33,33) =-26.67	a(34,30) =0.56	a(34,34) =-0.56	a(35,34) =0.06	a(35,35) =-0.06
a(36,30) =0.56	a(36,36) =-0.56	a(37,36) =0.67	a(37,37) =-0.67		

B. MATRIX B

b(4,3) = -0.001	b(5,3) = -0.001	b(7,3) = -0.03	b(8,3) = -0.03	b(10,3) = -0.07
b(11,3) = -0.07	b(14,3) = -0.0067	b(15,3) = -0.0067	$b(16,3) = -6.9 \cdot 10^{-7}$	$b(18,3) = -6.6 \cdot 10^{-18}$
$b(19,3) = 5.02 \cdot 10^{-4}$	$b(20,3) = 5.02 \cdot 10^{-4}$	b(22,4) = -0.015	b(23,4) = -0.015	b(25,3) = 0.0011
b(26,3) = 0.0011	b(28,4) = -0.0176	b(29,2) = 1.4	b(29,4) = -0.0176	$b(30,3) = -7.84 \cdot 10^{-18}$
b(31,1) = 469.55	b(32,3) = -0.27	b(33,3) = -0.27	$b(34,3) = -7.02 \cdot 10^{-18}$	$b(35,3) = -6.69 \cdot 10^{-18}$
$b(36,3) = -7.1 \cdot 10^{-18}$				

C. MATRIX C

c(1,31) = 1 c(2,16) = 1 c(3,22) = 1 c(4,18) = 1 c(5,30) = 1

APPENDIX B: $U^T R^* U$

$$
\begin{aligned}
U^T R^* U &= r_w \lim_{N_p \to \infty} \sum_{m=0}^{N_p} u(k_i+m)^T u(k_i+m) \\
&\to r_w \lim_{N_p \to \infty} \sum_{m=0}^{N_p} \eta^T L(m) L^T(m) \eta \\
&\to r_w \lim_{N_p \to \infty} \sum_{m=0}^{N_p} \eta^T \begin{bmatrix} L_1(m) & 0_1 & \cdots & 0_1 \\ 0_2 & L_2(m) & \cdots & 0_2 \\ \vdots & \vdots & \ddots & \vdots \\ 0_v & 0_v & \cdots & L_v(m) \end{bmatrix} \begin{bmatrix} L_1(m)^T & 0_2^T & \cdots & 0_v^T \\ 0_1^T & L_2(m)^T & \cdots & 0_v^T \\ \vdots & \vdots & \ddots & \vdots \\ 0_1^T & 0_2^T & \cdots & L_v(m)^T \end{bmatrix} \eta \\
&\to r_w \eta^T \begin{bmatrix} \lim_{N_p \to \infty} \sum_{m=0}^{N_p} L_1(m) L_1(m)^T & 0 & \cdots & 0 \\ 0 & \lim_{N_p \to \infty} \sum_{m=0}^{N_p} L_2(m) L_2(m)^T & \cdots & 0 \\ \vdots & \vdots & \ddots & \vdots \\ 0 & 0 & \cdots & \lim_{N_p \to \infty} \sum_{m=0}^{N_p} L_v(m) L_v(m)^T \end{bmatrix} \eta \\
&\to r_w \eta^T \begin{bmatrix} I_{N_1} & 0 & \cdots & 0 \\ 0 & I_{N_2} & \cdots & 0 \\ \vdots & \vdots & \ddots & \vdots \\ 0 & 0 & \cdots & I_{N_v} \end{bmatrix} \eta \\
\therefore U^T R^* U &= \eta^T (r_w I_{\sum N_i}) \eta = \eta^T R_L \eta.
\end{aligned}
$$

ACKNOWLEDGMENT

The authors would like to thank the Federal University of Mato Grosso do Sul, the National Council for Scientific and Technological Development (CNPq), the Oak Ridge National Laboratory (ORNL), the Coordination for the Improvement of Higher Education Personnel (CAPES), and the Research and Development Project—P&D ANEEL PD-06961-0010/2019.

REFERENCES

[1] S. R. Perillo and B. R. Upadhyaya, "Control and instrumentation strategies for multi-modular integral nuclear reactor systems," *IEEE Trans. Nucl. Sci.*, vol. 58, no. 5, pp. 2442–2451, Oct. 2011.

[2] J. Hines, B. R. Upadhyaya, J. M. Doster, and R. M. Edwards, "Advanced instrumentation and control methods for small and medium reactors with IRIS demonstration," Univ. Tennessee, Knoxville, TN, USA, Tech. Rep., 2011.

[3] J. B. Coble, B. R. Upadhyaya, C. Briere, C. Walker, A. O'Connor, J. W. Hines, Y.-C. Ko, and J. Ding, *Advanced Control Algorithms for Liquid Metal Reactors*. Knoxville, TN, USA: Univ. Tennessee, 2015.

[4] R. C. Berkan and B. R. Upadhyaya, *Dynamic Modeling of EBR-II for Simulation and Control*. Knoxville, TN, USA: Univ. Tennessee, 1988.

[5] Y. Xu, J. Liu, J. Yu, and Q.-G. Wang, "Adaptive neural networks command filtered control for MIMO nonlinear discrete-time systems with input constraint," *IEEE Trans. Circuits Syst. II, Exp. Briefs*, vol. 70, no. 2, pp. 581–585, Feb. 2023, doi: 10.1109/TCSII.2022.3170867.

[6] O. Saleem, F. Abbas, and J. Iqbal, "Complex fractional-order LQIR for inverted-pendulum-type robotic mechanisms: Design and experimental validation," *Mathematics*, vol. 11, no. 4, p. 913, Feb. 2023, doi: 10.3390/math11040913.

[7] O. Saleem and K. Mahmood-ul-Hasan, "Hierarchical adaptive control of self-stabilizing electromechanical systems using artificial-immune self-tuning mechanism for state weighting-factors," *J. Mech. Sci. Technol.*, vol. 35, no. 3, pp. 1235–1250, Mar. 2021, doi: 10.1007/s12206-021-0237-5.

[8] X. Liu, "Modeling and simulation of a prototypical advanced reactor," M.S. thesis, Univ. TN, USA, 2015. [Online]. Available: https://trace.tennessee.edu/utk/3595

[9] M. Zarei, "A multi-point kinetics based MIMO-PI control of power in PWR reactors," *Nucl. Eng. Design*, vol. 328, pp. 283–291, Mar. 2018, doi: 10.1016/j.nucengdes.2018.01.011.

[10] N. Zare, G. Jahanfarnia, A. Khorshidi, and J. Soltani, "Robustness of optimized FPID controller against uncertainty and disturbance by fractional nonlinear model for research nuclear reactor," *Nucl. Eng. Technol.*, vol. 52, no. 9, pp. 2017–2024, Sep. 2020, doi: 10.1016/j.net.2020.03.002.

[11] G. Wang, J. Wu, B. Zeng, Z. Xu, W. Wu, and X. Ma, "State-space model predictive control method for core power control in pressurized water reactor nuclear power stations," *Nucl. Eng. Technol.*, vol. 49, no. 1, pp. 134–140, Feb. 2017, doi: 10.1016/j.net.2016.07.008.

[12] W. Zeng, W. Zhu, T. Hui, L. Chen, J. Xie, and T. Yu, "An IMC-PID controller with particle swarm optimization algorithm for MSBR core power control," *Nucl. Eng. Des.*, vol. 360, Apr. 2020, Art. no. 110513, doi: 10.1016/j.nucengdes.2020.110513.

[13] O. Safarzadeh and O. Noori-kalkhoran, "A fractional PID controller based on fractional point kinetic model and particle swarm optimization for power regulation of SMART reactor," *Nucl. Eng. Des.*, vol. 377, Jun. 2021, Art. no. 111137, doi: 10.1016/j.nucengdes.2021.111137.

[14] F. Bostelmann, G. Ilas, and W. A. Wieselquist, "Nuclear data sensitivity study for the EBR-II fast reactor benchmark using SCALE with ENDF/B-VII.1 and ENDF/B-VIII.0," *J. Nucl. Eng.*, vol. 2, no. 4, pp. 345–367, Sep. 2021, doi: 10.3390/jne2040028.

[15] C. Pope and E. Lum, "Nuclear reactor thermal expansion reactivity effect determination using finite element analysis coupled with Monte Carlo neutron transport analysis," in *Finite Element Methods and Their Applications*. London, United Kingdom: IntechOpen, 2020. [Online]. Available: https://www.intechopen.com/chapters/73425, doi: 10.5772/intechopen.93762.

[16] G. Bengtsson, "Output regulation and internal models—A frequency domain approach," *Automatica*, vol. 13, no. 4, pp. 333–345, 1977.

[17] R. Cordero, T. Estrabis, E. A. Batista, C. Q. Andrea, and G. Gentil, "Ramp-tracking generalized predictive control system-based on second-order difference," *IEEE Trans. Circuits Syst. II, Exp. Briefs*, vol. 68, no. 4, pp. 1283–1287, Apr. 2021.

[18] R. Cordero, T. Estrabis, G. Gentil, E. A. Batista, and C. Q. Andrea, "Development of a generalized predictive control system for polynomial reference tracking," *IEEE Trans. Circuits Syst. II, Exp. Briefs*, vol. 68, no. 8, pp. 2875–2879, Aug. 2021, doi: 10.1109/TCSII.2021.3058625.

[19] R. Cordero, T. Estrabis, M. A. Brito, and G. Gentil, "Development of a resonant generalized predictive controller for sinusoidal reference tracking," *IEEE Trans. Circuits Syst. II, Exp. Briefs*, vol. 69, no. 3, pp. 1218–1222, Mar. 2022, doi: 10.1109/TCSII.2021.3102535.

[20] T. Su, L. Cheng, Y. Wang, X. Liang, J. Zheng, and H. Zhang, "Time-optimal trajectory planning for delta robot based on quintic pythagorean-hodograph curves," *IEEE Access*, vol. 6, pp. 28530–28539, 2018.

[21] R. C. Garcia, J. O. P. Pinto, W. I. Suemitsu, and J. O. Soares, "Improved demultiplexing algorithm for hardware simplification of sensored vector control through frequency-domain multiplexing," *IEEE Trans. Ind. Electron.*, vol. 64, no. 8, pp. 6538–6548, Aug. 2017.

[22] C. Liu, J. Jiang, J. Jiang, and Z. Zhou, "Enhanced grid-connected phase-locked loop based on a moving average filter," *IEEE Access*, vol. 8, pp. 5308–5315, 2020.

[23] A. Bamigbade, V. Khadkikar, and M. Al Hosani, "A type-3 PLL for single-phase applications," *IEEE Trans. Ind. Appl.*, vol. 56, no. 5, pp. 5533–5542, Sep./Oct. 2020.

[24] K. G. Papadopoulos, E. N. Papastefanaki, and N. I. Margaris, "Explicit analytical PID tuning rules for the design of type-III control loops," *IEEE Trans. Ind. Electron.*, vol. 60, no. 10, pp. 4650–4664, Oct. 2013.

[25] L. Wang, *From Plant Data to Process Control: Ideas for Process Identification and PID Design*. Boca Raton, FL, USA: CRC Press, 2014.

[26] P. M. Makila and J. R. Partington, "Laguerre and Kautz shift approximations of delay systems," *Int. J. Control*, vol. 72, no. 10, pp. 932–946, Jan. 1999.

[27] E. Sobhani Tehrani and R. E. Kearney, "A non-parametric approach for identification of parameter varying Hammerstein systems," *IEEE Access*, vol. 10, pp. 6348–6362, 2022, doi: 10.1109/ACCESS.2022.3141704.

[28] J. A. Rossiter, L. Wang, and G. Valencia-Palomo, "Efficient algorithms for trading off feasibility and performance in predictive control," *Int. J. Control*, vol. 83, no. 4, pp. 789–797, Apr. 2010.

[29] L. F. da S. C. Pereira, E. A. Batista, J. O. P. Pinto, B. R. Upadhyaya, J. W. Hines, and J. B. Coble, "Model predictive control for sodium fast reactors based on Laguerre functions and FPGA-in-the-loop environment," *Nucl. Eng. Des.*, vol. 400, Dec. 2022, Art. no. 112041, doi: 10.1016/j.nucengdes.2022.112041.

[30] G. B. Price, "Telescoping sums and the summation of sequences," *Two-Year College Math. J.*, vol. 4, no. 2, pp. 16–29, Spring 1973.

[31] S. Boyd and L. Vandenberghe, *Introduction to Applied Linear Algebra: Vectors, Matrices, and Least Squares*. Cambridge, U.K.: Cambridge Univ. Press, 2018, pp. 206–208.

[32] T. O. Silva, *Laguerre Filters: An Introduction*. 1995.

[33] J. Saeed, L. Wang, and N. Fernando, "Model predictive control of phase shift full-bridge DC–DC converter using Laguerre functions," *IEEE Trans. Control Syst. Technol.*, vol. 30, no. 2, pp. 819–826, Mar. 2022, doi: 10.1109/TCST.2021.3069148.

[34] A. V. Medvedev, V. Bro, and R. Ushirobira, "Linear time-invariant discrete delay systems in Laguerre domain," *IEEE Trans. Autom. Control*, vol. 67, no. 5, pp. 2677–2683, May 2022, doi: 10.1109/TAC.2021.3096927.

[35] A. Dubravi, Z. Šeh, and M. Burgić, "Orthonormal functions based model predictive control of pH neutralization process," *Tech. Gazette*, vol. 21, no. 6, pp. 1249–1253, 2014.

[36] D. Jeong and S. B. Choi, "Tracking control based on model predictive control using Laguerre functions with pole optimization," *IEEE Trans. Intell. Transp. Syst.*, vol. 23, no. 11, pp. 20652–20663, Nov. 2022, doi: 10.1109/TITS.2022.3179613.

[37] A. Dubravi and Z. Šehi, "Using orthonormal functions in model predictive control," *Tech. Gazette*, vol. 19, no. 3, pp. 513–520, 2012.

[38] L. Wang, *Model Predictive Control System Design and Implementation Using MATLAB*, 1st ed. Springer, 2009.

[39] A. Aures, F. Bostelmann, A. Ivan Kodeli, K. Velkov, and W. Zwermann, "Uncertainty in the delayed neutron fraction in fuel assembly depletion calculations," in *Proc. EPJ Web Conf.*, vol. 146, 2017, p. 02052, doi: 10.1051/epjconf/201714602052.

[40] T. M. Sembiring, "Evaluation of the AP1000 delayed neutron parameters using MCNP6," in *Proc. J. Phys., Conf.*, vol. 962, 2018, Art. no. 012030, doi: 10.1088/1742-6596/962/1/012030.

LUÍS FELIPE DA SILVA CARLOS PEREIRA was born in Campo Grande, Mato Grosso do Sul, Brazil. He received the degree in communication engineering from the Military Institute of Engineering (IME), in 2016, and the M.Sc. degree in electrical engineering from the Federal University of Mato Grosso do Sul, in 2022. He is currently an Associate Engineer with the Brazilian Army. His main publications are related to applications in model predictive control and fractional-order control. His research interests include advanced control methods, signal processing, power-electronics systems, real-time hardware-in-the-loop simulation, and VHDL coding.

EDSON ANTONIO BATISTA (Member, IEEE) was born in Ilha Solteira, São Paulo, Brazil. He received the B.Sc., M.Sc., and Ph.D. degrees in electrical engineering from Universidade Estadual Paulista Júlio de Mesquita Filho (UNESP/FEIS), in 2001, 2004, and 2009, respectively.

From 2015 to 2016, he was a Postdoctoral Researcher with the Department of Nuclear Engineering, University of Tennessee, USA. He is currently an Adjunct Professor with FAENG, Federal University of Mato Grosso do Sul (UFMS), and a Coordinator of the Embedded Systems Laboratory, which contains projects funded by CNPq, P&D Aneel, and FUNDECT/MS. He is a Coordinator of the Graduate Program in Electrical Engineering, UFMS. His research areas involve smart grids, intelligent instrumentation based on the concepts of the IEEE 1451 standard, real-time hardware-in-the-loop simulation, model predictive control, and fractional-order derivative application in hardware development. He is also a Reviewer of the *Journal of Control, Automation and Electrical Systems*.

JOÃO ONOFRE PEREIRA PINTO (Senior Member, IEEE) was born in Valparaiso, Brazil. He received the B.S. degree in electrical engineering from Universidade Estadual Paulista, Brazil, in 1990, the M.S. degree from Universidade Federal de Uberlândia, Brazil, in 1993, and the Ph.D. degree from the University of Tennessee, Knoxville, TN, USA, in 2001. He was a Faculty Member with the Federal University of Mato Grosso do Sul (UFMS), Campo Grande, Brazil, from 1994 to 2021, where he was the Dean of the Engineering College, from 2013 to 2017. He was the Founder and the Director of BATLAB, artificial intelligence applications, power electronics and drives, and energy systems. He has been a Faculty Member with the Federal University of Rio de Janeiro, Rio de Janeiro, Brazil, on leave of absence, since 2021. He is currently a Senior Researcher with the Oak Ridge National Laboratory, Oak Ridge, TN, USA. He has more than 200 published papers in journals and conference proceedings. His research interests include power electronics, artificial intelligence applications, energy systems, and electrical machine drives.

BELLE R. UPADHYAYA received the Ph.D. degree in engineering sciences (systems science) from the University of California at San Diego.

He is currently a Professor Emeritus of nuclear engineering with the University of Tennessee, Knoxville, TN, USA. He has published more than 370 papers in scientific journals and conference proceedings and chapters in handbooks. He is the author or coauthor of more than 150 research reports. His research and teaching interests include instrumentation and controls, reactor dynamics, advanced digital signal processing, power and process plant monitoring and diagnosis, autonomous and fault-tolerant control, small modular reactors, integral light water reactors, sodium fast reactors, nuclear desalination, sensor placement strategies, accelerated aging of detectors and equipment, nondestructive examination, and reliability and maintainability engineering.

J. WESLEY HINES received the B.S. degree in electrical engineering from Ohio University, in 1985, and the M.B.A., M.S., and Ph.D. degrees in nuclear engineering from The Ohio State University, in 1992 and 1994, respectively. He was a Nuclear Qualified Submarine Officer with the USA Navy. He was the Interim Associate Dean for Research with the College of Engineering and more recently an Interim Vice Chancellor for Research. He is currently the Head of the Nuclear Engineering Department, University of Tennessee, Knoxville, TN, USA. He has authored more than 275 articles and has three patents that have been implemented in commercial products.